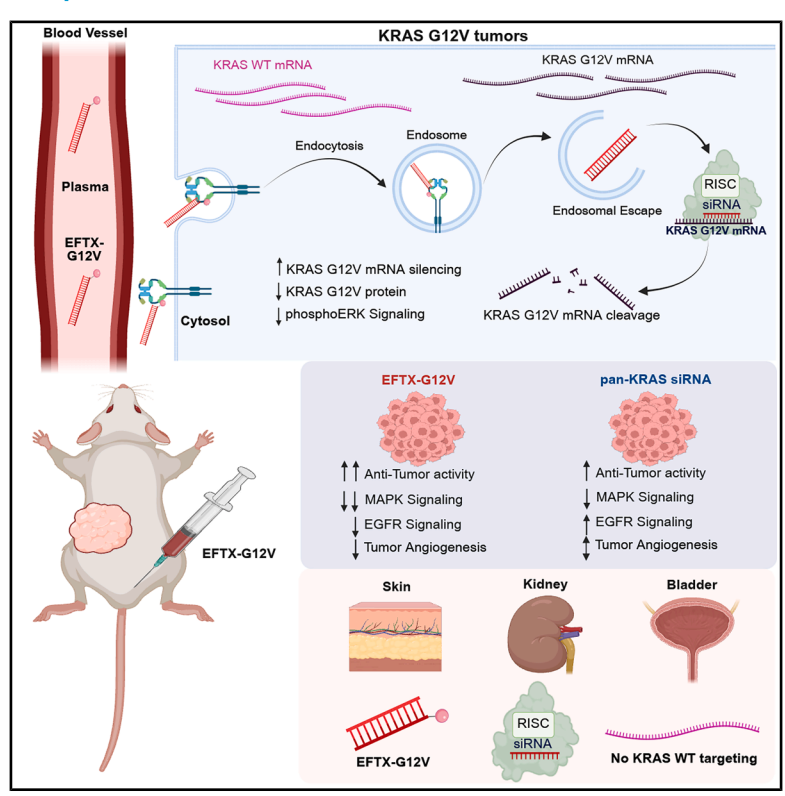
# **Cancer Cell**

# A first-in-class EGFR-directed KRAS G12V selective inhibitor

# **Graphical abstract**



### **Authors**

Lyla J. Stanland, Hayden P. Huggins, Snehasudha S. Sahoo, ..., Martin Egli, Albert A. Bowers, Chad V. Pecot

# Correspondence

pecot@email.unc.edu

### In brief

Despite KRAS G12V being a common mutation in cancer, no direct inhibitors currently exist. Stanland et al. demonstrate that an EGFR-directed RNAi platform, EFTX-G12V, selectively targets KRAS G12V while sparing wild-type KRAS. EFTX-G12V shows significant antitumor effects and provides insights into mutant-selective KRAS targeting and improved therapeutic activity.

# **Highlights**

- EFTX-G12V is a highly potent mutant-selective siRNA inhibitor of KRAS G12V
- Delivery of EFTX-G12V by EGFR-targeting improves tumorto-normal payload delivery
- EFTX-G12V inhibits tumor growth in lung, colon, and pancreatic cancer models
- EFTX-G12V outperforms pan-KRAS siRNA in vivo through unique signaling mechanisms





# **Cancer Cell**



# **Article**

# A first-in-class EGFR-directed KRAS G12V selective inhibitor

Lyla J. Stanland, <sup>1,14</sup> Hayden P. Huggins, <sup>1,2,14</sup> Snehasudha S. Sahoo, <sup>2,3</sup> Alessandro Porrello, <sup>2,3</sup> Yogitha Chareddy, <sup>2,3,4</sup> Salma H. Azam, <sup>2</sup> Jillian L. Perry, <sup>2,5,6</sup> Pradeep S. Pallan, <sup>7</sup> Kristina Whately, <sup>2,3</sup> Lincy Edatt, <sup>2,3</sup> William D. Green, <sup>2,8</sup> Matthew C. Fleming, <sup>6,9</sup> Jonah Im, <sup>1,2</sup> Christina Gutierrez-Ford, <sup>2</sup> Imani Simmons, <sup>2</sup> Alyaa Dawoud, <sup>2,3</sup> Katherine I. Zhou, <sup>2,3,10</sup> Vandanaa Jayaprakash, <sup>1,2</sup> Rani S. Sellers, <sup>11</sup> Gabriela de la Cruz, <sup>11</sup> Albert Wielgus, <sup>11</sup> Justin Milner, <sup>2,8</sup> Martin Egli, <sup>7</sup> Albert A. Bowers, <sup>2,3,6,9,12</sup> and Chad V. Pecot<sup>2,3,13,15,\*</sup>

#### **SUMMARY**

Despite *KRAS*<sup>G12V</sup> being the second most common *KRAS* mutation in cancer, no direct inhibitors targeting KRAS<sup>G12V</sup> have been approved. RNA interference (RNAi) has faced numerous obstacles as cancer therapeutic, including the lack of cancer-specific tissue targeting, rapid oligonucleotide nuclease degradation, and clearance from circulation. Recently, the use of targetable ligands conjugated to chemically modified siRNAs have shown remarkable promise in circumventing these barriers. In this study, we demonstrate that an EGFR-directed RNAi molecule (EFTX-G12V) is highly selective for *KRAS*<sup>G12V</sup> and exhibits improved therapeutic activity over pan-KRAS targeting, including enhanced inhibition of several cancer hallmarks. Using a targeted RNAi delivery platform, we achieve effective tumor silencing of *KRAS*<sup>G12V</sup> and significant anti-tumor activity across several cancer models. Our findings represent a technological advance in oncogene targeting using RNAi and provide new biologic insights in KRAS targeting with potential implications for safety and efficacy.

### INTRODUCTION

The *Kirsten rat sarcoma* (*KRAS*) proto-oncogene encodes a small GTPase that is crucial for the activation of numerous intracellular signaling pathways that regulate cell proliferation, survival, and differentiation. Missense mutations in *KRAS* often result in its constitutive activation, leading to dysregulated downstream signaling cascades that drive oncogenic transformation. As such, *KRAS* mutations are present in nearly 25% of all human cancers, and they frequently occur in some of the most prevalent cancer types, such as lung (35%), colorectal (49%), and pancreatic adenocarcinomas (92%).

Activating KRAS mutations are well defined and typically occur in one of three major hotspots located at codons 12, 13,

and 61, where they impair GTPase activity resulting in increased GTP-bound active KRAS. Across cancer populations, KRAS G12D (29%), G12V (23%), G12C (15%), and G13D (7%) are the most common mutations,  $^1$  and for reasons that remain poorly understood, some KRAS mutations occur at a higher frequency in certain cancer subtypes. For example, the G12D mutation is the most common in pancreatic (42%) and colon (30%) cancers, while the G12C mutation is most common in lung cancer (40%). The clinical prevalence and significance of activating KRAS mutations underscores the importance of developing targeted therapies to specific mutations.

Until recently, KRAS was viewed as "undruggable" with traditional small molecule inhibitor approaches due to its pM affinity for GTP, undesirable surface topology, and lack of a hydrophobic



<sup>&</sup>lt;sup>1</sup>EnFuego Therapeutics, Inc., Morrisville, NC 27560, USA

<sup>&</sup>lt;sup>2</sup>Lineberger Comprehensive Cancer Center, University of North Carolina (UNC) at Chapel Hill, Chapel Hill, NC, USA

<sup>&</sup>lt;sup>3</sup>RNA Discovery Center, UNC at Chapel Hill, Chapel Hill, NC, USA

<sup>&</sup>lt;sup>4</sup>Curriculum in Genetics and Molecular Biology, UNC at Chapel Hill, Chapel Hill, NC, USA

<sup>&</sup>lt;sup>5</sup>Center for Nanotechnology in Drug Delivery, Chapel Hill, NC, USA

<sup>&</sup>lt;sup>6</sup>Division of Chemical Biology and Medicinal Chemistry, UNC at Chapel Hill, Chapel Hill, NC, USA

<sup>&</sup>lt;sup>7</sup>Department of Biochemistry, Vanderbilt University, Nashville, TN 37232, USA

<sup>&</sup>lt;sup>8</sup>Department of Microbiology and Immunology, UNC at Chapel Hill, Chapel Hill, NC, USA

<sup>&</sup>lt;sup>9</sup>Center for Integrative Chemical Biology and Drug Discovery, Chapel Hill, NC, USA

<sup>&</sup>lt;sup>10</sup>Division of Medical Oncology, Duke University, Durham, NC 27705, USA

<sup>&</sup>lt;sup>11</sup>Department of Pathology and Laboratory Medicine, UNC at Chapel Hill, Chapel Hill, NC, USA

<sup>&</sup>lt;sup>12</sup>Department of Chemistry, UNC at Chapel Hill, Chapel Hill, NC, USA

<sup>&</sup>lt;sup>13</sup>Division of Hematology/Oncology, UNC at Chapel Hill, Chapel Hill, NC, USA

<sup>&</sup>lt;sup>14</sup>These authors contributed equally

<sup>15</sup>Lead contact

<sup>\*</sup>Correspondence: pecot@email.unc.edu https://doi.org/10.1016/j.ccell.2025.05.016



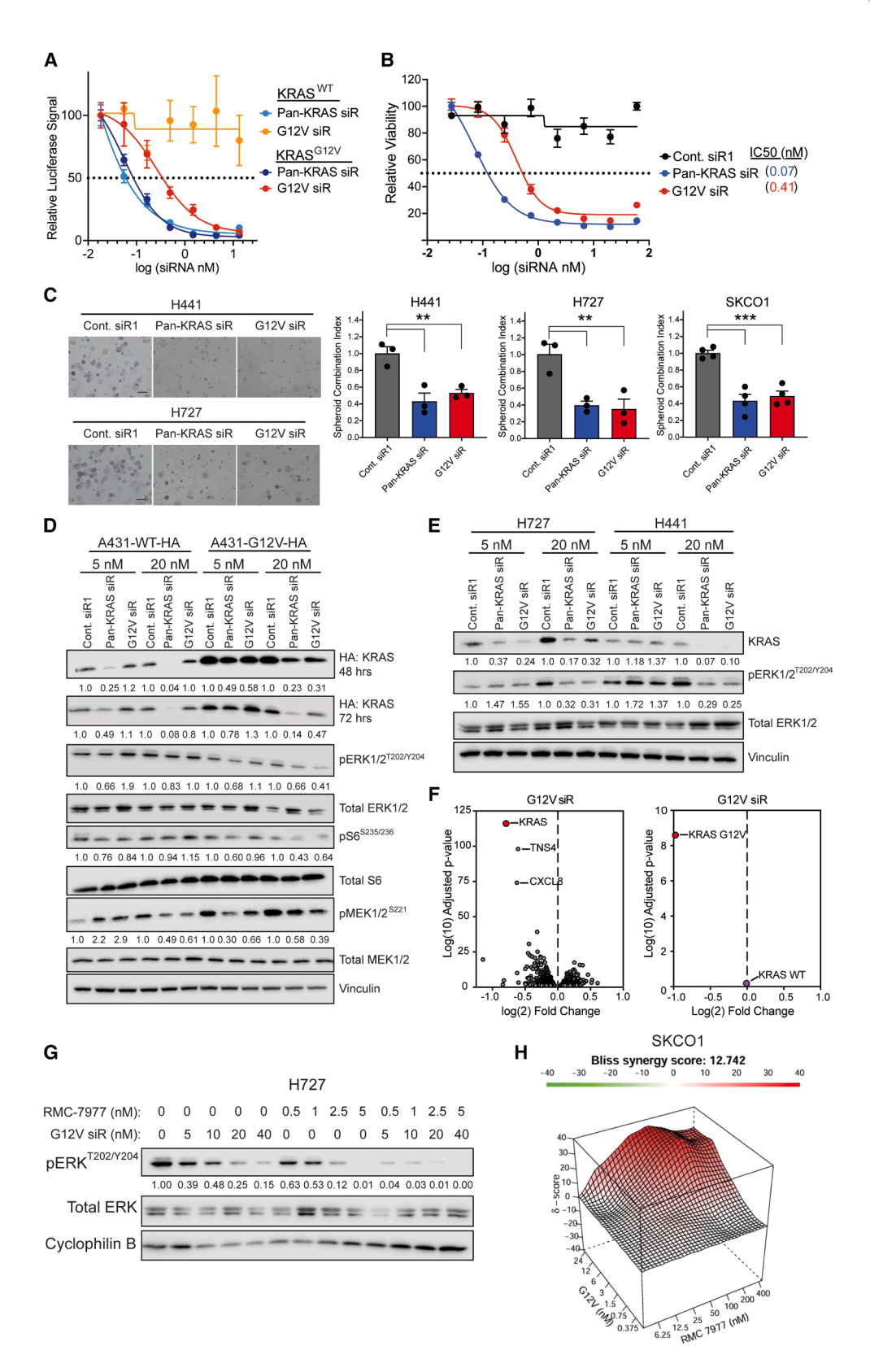


Figure 1. Discovery, SAR and validation of KRAS G12V specific siRNA in vitro

(A) 7-point Luciferase dose-response curve in A431-KRAS-WT or -KRAS-G12V cells stably expressing a luciferase reporter.

(B) 8-point dose-response curve in SKCO1 cells.



core. However, recent advancements in structural and computational biology and new chemical approaches have renewed interest in targeting mutant KRAS resulting in the approval of two KRAS<sup>G12C</sup> inhibitors now used in the clinic, sotorasib and adagrasib, 3,4 and additional inhibitors are in clinical development. 5,6 Further, non-covalent KRAS<sup>G12D</sup> specific (MRTX1133 and HRS-4642),<sup>7,8</sup> covalent KRAS<sup>G12D,9</sup> pan-KRAS (BI-2865),<sup>10</sup> and pan-RAS (clinical candidate: RMC-6236, pre-clinical molecule: RMC-7977)<sup>11-13</sup> inhibitors are at various stages of clinical development. The latter molecules target all tested KRAS mutations and represent the potential for a broad clinical impact. However, because pan-KRAS/-RAS strategies simultaneously target KRAS wild-type (WT), the therapeutic window is anticipated to be narrower, and the biologic effects of targeting  $KRAS^{WT}$  within KRAS mutant tumors remains poorly understood. 14 Despite the substantial progress in developing KRAS inhibitors over the past decade, there remains no direct KRAS<sup>G12V</sup> inhibitors in the clinic.

Together, the clinical significance and chemical intractability of the KRAS<sup>G12V</sup> mutation demand new molecular interventions. Until recently, the prospects of using RNAi therapeutics in the cancer clinic have seemed dire. However, as evidenced by the first FDA-approved ligand-conjugated siRNA drug (givosiran), <sup>15</sup> the promise of therapeutic RNAi in the cancer clinic will largely depend on whether sufficient tumor delivery and target engagement is possible. <sup>16,17</sup> Here, we demonstrate an EGFR-directed, highly specific RNAi molecule (EFTX-G12V) that selectively inhibits *KRAS*<sup>G12V</sup> expression and results in significant preclinical activity. Our findings represent a powerful technological advancement in mutant-selective oncogene therapeutics using RNA interference (RNAi) and reveal important biological insights into KRAS targeting that have broader clinical implications with regards to toxicity and therapeutic efficacy.

### **RESULTS**

#### Development of a KRAS G12V selective siRNA molecule

Previously, we used an engineered artificial *KRAS* mRNA sequence to design unmodified siRNAs capable of targeting *KRAS*<sup>G12C</sup>, *KRAS*<sup>G12V</sup>, and *KRAS*<sup>G13D</sup> mutations while sparing *KRAS*<sup>WT</sup>. <sup>18</sup> We designed three versions of fully modified *KRAS*<sup>G12V</sup> mutant-specific siRNAs each with a mixture of 2'Fluoro (2'F) and 2'-O-methyl (2'-O-Me) ribose modifications throughout the sense and antisense strands, as well as phosphorothioate (PS) linkages at the 5' and 3' termini of each strand. These modifications substantially improve endo- and exonuclease resistance, enhance thermodynamic properties, decrease immunogenicity, and potentially reduce off-target effects; thus, conferring desirable drug-like properties. <sup>17,19-21</sup> To

assess these designs, we performed a viability dose-response curve on *KRAS*<sup>G12V</sup> mutant SKCO1 colon cancer cells and found that two of the designs exhibited low nanomolar potency (Figure S1A).

To evaluate the mutant selectivity of these two designs, siRNAs were transfected into isogenic A431 cells expressing either HA-tagged *KRAS*<sup>WT</sup> or *KRAS*<sup>G12V</sup>. <sup>18</sup> Compared to a nontargeting control siRNA (control siR1), both siRNAs decreased *KRAS* mRNA expression to similar levels as a pan-KRAS siRNA. <sup>22</sup> However, only one siRNA demonstrated robust *KRAS*<sup>WT</sup> sparing and was therefore nominated for further evaluation (Figure S1B).

Previous studies have shown that the number and placement of 2'-F and 2'-O-Me modifications have a significant effect on siRNA stability and efficacy in vivo. 20,21,23-25 Building on our best performing siRNA molecule that has a higher number of 2'-F modifications (Hi2F), we evaluated designs that were higher in 2'-O-Me modifications (Hi2OMe). Notable advantages of increasing 2'-O-Me content in an siRNA include reduced offtarget effects and immunogenicity, and improved allele-specific targeting and nuclease resistance. 23,24,26 Using isogenic A431 cells engineered to express either KRASWT or KRASG12V fused to a luciferase reporter, we evaluated dose-responses following transfection with either the Hi2F or Hi2OMe siRNA molecule. As expected, pan-KRAS siRNA equally inhibited KRAS G12V and KRASWT expression. The Hi2F design reduced KRASG12V activity similarly to pan-KRAS siRNA but also led to  $\sim$ 50% reduction of KRASWT activity. Conversely, the Hi2OMe design potently inhibited KRAS G12V activity while completely sparing KRAS WT activity (Figures 1A and S1C). We therefore moved forward with the Hi2OMe design given its greater specificity for KRAS<sup>G12V</sup>.

We performed a dose-response experiment in SKCO1 cells and found that G12V siRNA potently inhibited cell growth with a GI  $_{50}$  value of 0.41 nM (Figure 1B). We then evaluated 3D spheroid growth to model impact on tumorigenesis and observed significant reductions in total spheroid number and size with both pan-KRAS siRNA and G12V siRNA in all three models tested (Figure 1C).

We next evaluated KRAS protein expression and downstream MAPK signaling following siRNA transfection in the A431 isogenic KRAS HA-tagged cell lines. After 48 h, relative to control siRNA, G12V siRNA had no effect on KRAS protein expression in *KRAS*<sup>WT</sup> cells but resulted in a 42% and 69% knockdown of KRAS protein at 5 nM and 20 nM, respectively, in *KRAS*<sup>G12V</sup> cells (Figure 1D). After 72 h, G12V siRNA still elicited minimal reduction of KRAS protein in *KRAS*<sup>WT</sup> cells, while resulting in a 53% reduction of KRAS protein at 20 nM in *KRAS*<sup>G12V</sup> cells. We also observed that *KRAS*<sup>G12V</sup> cells treated with G12V siRNA

<sup>(</sup>C) 3D growth of cells embedded in Matrigel after transfection with siRNAs at 20 nM. Spheroids were imaged after 8 days of growth, and conditions were run in at least triplicate, scale bar 200  $\mu$ M.

<sup>(</sup>D) Western blot analysis in A431 cells stably expressing KRAS<sup>WT</sup> or -G12V transiently transfected with siRNAs. Cells were analyzed at 48 h and 72 h. Blots were done separately, and quantification is based on vinculin control for each individual blot. Representative vinculin blot shown.

<sup>(</sup>E) Western blot analysis in cells transiently transfected with siRNAs. Cells were analyzed at 72 h. Quantification is based on vinculin control.

<sup>(</sup>F) Volcano plots from RNA-sequencing in SKCO1 cells transiently transfected with siRNAs at 20 nM. Cells were analyzed at 24 h.

<sup>(</sup>G) Western blot analysis in cells transfected with G12V siRNA or treated with RMC-7977 alone and in combination. Cells were analyzed at 24 and 72 h and quantification is based on cyclophilin B.

<sup>(</sup>H) 3D representation of Bliss Synergy score. All data points measured in at least triplicate and shown as mean  $\pm$  S.E.M. Statistical significance was measured by one-way ANOVA test; p-values \*p < 0.01, \*\*\*p < 0.01, \*\*\*p < 0.005. See also Figure S1.



exhibited decreased downstream signaling in multiple effectors including pERK1/2  $^{T202/Y204}$ , pS6  $^{S235/236}$  and pMEK1/2  $^{S221}$  (Figure 1D). Additionally, KRAS  $^{G12V}$  mutant H727 and H441 cells treated with G12V siRNA exhibited a  $\sim\!70\text{--}90\%$  decrease in KRAS protein at 5 nM and 20 nM, with a corresponding  $\sim\!70\text{--}75\%$  decrease in pERK1/2  $^{T202/Y204}$  at 20 nM (Figure 1E).

To further evaluate the specificity of KRAS<sup>G12V</sup> targeting, we measured KRAS and DUSP6 mRNA expression in a KRAS G12C mutant cell line, H358. G12V siRNA had no effect on gene expression, while pan-KRAS siRNA significantly decreased both KRAS and DUSP6 expression. (Figures S1D and S1E). We used RNA-sequencing to more rigorously evaluate potential off-target effects. We transfected SKCO1 cells, collected RNA after 24 h and looked for unintended off-target changes in gene expression. Besides KRAS, the next most significantly downregulated genes for both the pan-KRAS and G12V siRNAs were TNS4 and CXCL8, both of which are reported downstream effectors of KRAS-mutant cancer and are indeed on-target (Figure 1F, left; Figure S1F). 27,28 Because SKCO1 is a heterozygous KRAS<sup>G12V</sup> mutant cell line, we then evaluated the siRNAs for their effects on each allele. We found that  $\mathit{KRAS}^{\mathit{G12V}}$  was significantly downregulated by G12V siRNA, while  $KRAS^{WT}$  was completely spared (Figure 1F, right). Conversely, as expected, in cells transfected with pan-KRAS siRNA, both KRAS<sup>G12V</sup> and KRAS<sup>WT</sup> were significantly and nearly equally downregulated (Figure S1G). Together, these data describe the development of a potent, highly KRAS<sup>G12V</sup> specific siRNA that is chemically modified to confer drug-like

Lastly, we posited that dual targeting of mutant KRAS at the mRNA and protein levels may more effectively ablate downstream MAPK signaling than either modality alone. We evaluated the potential of combining G12V siRNA with RMC-7977, a small molecule pan-RAS inhibitor. 15 Western blot analyses of  $\mathsf{pERK}^{\mathsf{T202/Y204}}$  showed that the combination of G12V siRNA and RMC-7977 enhanced MAPK silencing compared to each inhibitor alone in several cell lines (Figures 1G and S2A). We additionally completed dose-escalation viability experiments and found that in SKCO1 cells, the combination of G12V siRNA and RMC-7977 was synergistic (Figures 1H and S2D). In H727 cells, the combination was predominantly additive, resulting in enhanced inhibition compared to G12V siRNA as a single agent (Figures S2B and S2C). These data suggest that co-targeting KRAS at both the mRNA and protein levels out-perform each therapeutic modality as a single agent.

## Thermodynamics and modeling of the G12V siRNA

We investigated how G12V siRNA specifically targets *KRAS*<sup>G12V</sup> mRNA and spares *KRAS*<sup>WT</sup> mRNA, despite having only a single mismatch with the WT transcript at anti-sense (AS) position 5. Using UV melting experiments, we determined the melting temperature for the AS strand of G12V siRNA complexed with each of the different synthetic *KRAS* mRNA mimics for *KRAS*<sup>WT</sup>, *KRAS*<sup>G12D</sup> (which also has an AS5 mismatch), and *KRAS*<sup>G12V</sup>. The average melting temperatures for *KRAS*<sup>WT</sup> (A:G mismatch pair – 73.6°C) and *KRAS*<sup>G12D</sup> (A:A mismatch pair – 73.3°C) were nearly 6°C lower than for *KRAS*<sup>G12V</sup> (A:U matching pair – 79°C) (Figure 2A). These findings implicate differential thermodynamics as a mechanistic basis for mutant selectivity.

To study the structural implications of these 3 KRAS mRNA pairings with the G12V siRNA when loaded into Ago2, we performed in silico modeling. Whereas the G12V siRNA forms an A:U pair with KRAS at AS position 5 (Figure 2B), this standard Watson-Crick base pair is replaced by a purine-purine pair when G12V siRNA is bound to either KRASWT (Figure 2C) or KRAS<sup>G12D</sup> (Figure 2D). Replacing the C:G pair in the parent crystal structure of the Ago2-dsRNA complex with an A:U pair (G12D) is of little consequence for duplex conformation and interactions with Ago2. Indeed, the computational model of this complex shows intact H-bond formation and stacking between A:U and neighboring base pairs (Figure 2B). The changes relative to the parent complex are more pronounced in the simulated models of complexes with purine-purine pairs. For KRASWT, the model shows high propeller twist between A and G with locally diminished stacking, although the relative orientation of bases still permits two H-bonds (Figure 2C). For the G12D mutant, the adenine at AS5 appears to be even more rotated out of the plane defined by the sense strand adenine, and base pairing is reduced to one H-bond (Figure 2D). In both complex models with purine-purine pairs, the RNA duplex is widened by ca. 1 Å compared to that in the crystal structure. These geometric changes likely negatively affect the interactions with Ago2 and potentially further enhance the selectivity for KRAS G12V mutant over KRASWT and KRASG12D (Figure 2A). Overall, the thermal melting analysis and computer modeling afford a rationalization of the favorable potency of the G12V siRNA that is consistent with the results from cell-based activity assays.

#### **Development of an EGFR-directed RNAi platform**

A major factor limiting the widespread use of oligonucleotidebased drugs in oncology is the need for targeting moieties that can selectively and efficiently deliver oligo payloads to tumors. 17,29 One promising receptor is the epidermal growth factor receptor (EGFR), which is overexpressed in many carcinomas and was identified as one of the most attractive cancer-specific targets by single-cell RNA-sequencing.30 By evaluating the Broad's Cancer Cell Line Encyclopedia (CCLE), we confirmed across >600 cell lines that KRAS-mutated carcinomas frequently express high levels of EGFR (Figure 3A). We directly compared EGFR expression levels between >500 non-small cell lung cancer (NSCLC) tumors with a tissue microarray of 27 healthy somatic tissues. We used the H-scoring method to measure EGFR receptor expression, which takes into consideration both membranous staining intensity (ranked at 0, 1, 2, and 3) and the percentage of tumor cells with the correspondent intensity, giving a composite score between 0 and 300. We found the majority of NSCLC samples had EGFR H-scores of at least 60, while only a few somatic tissues (notably skin, bladder and small bowel) demonstrated EGFR H-scores >60 (Figures 3B and S3A). Based on these findings, we determined that EGFR is an attractive target with a high potential for tumor-to-normal payload delivery.

Previously, a 12 amino acid EGFR-targeting peptide (YHWYGYTPQNVI), called GE11, was discovered through phage display and demonstrated favorable binding kinetics to EGFR. <sup>31</sup> GE11 is non-mitogenic, and when conjugated it has been used as a targeting moiety for numerous purposes, including for enhancing nanoparticle delivery, imaging modalities, and *in vitro* 



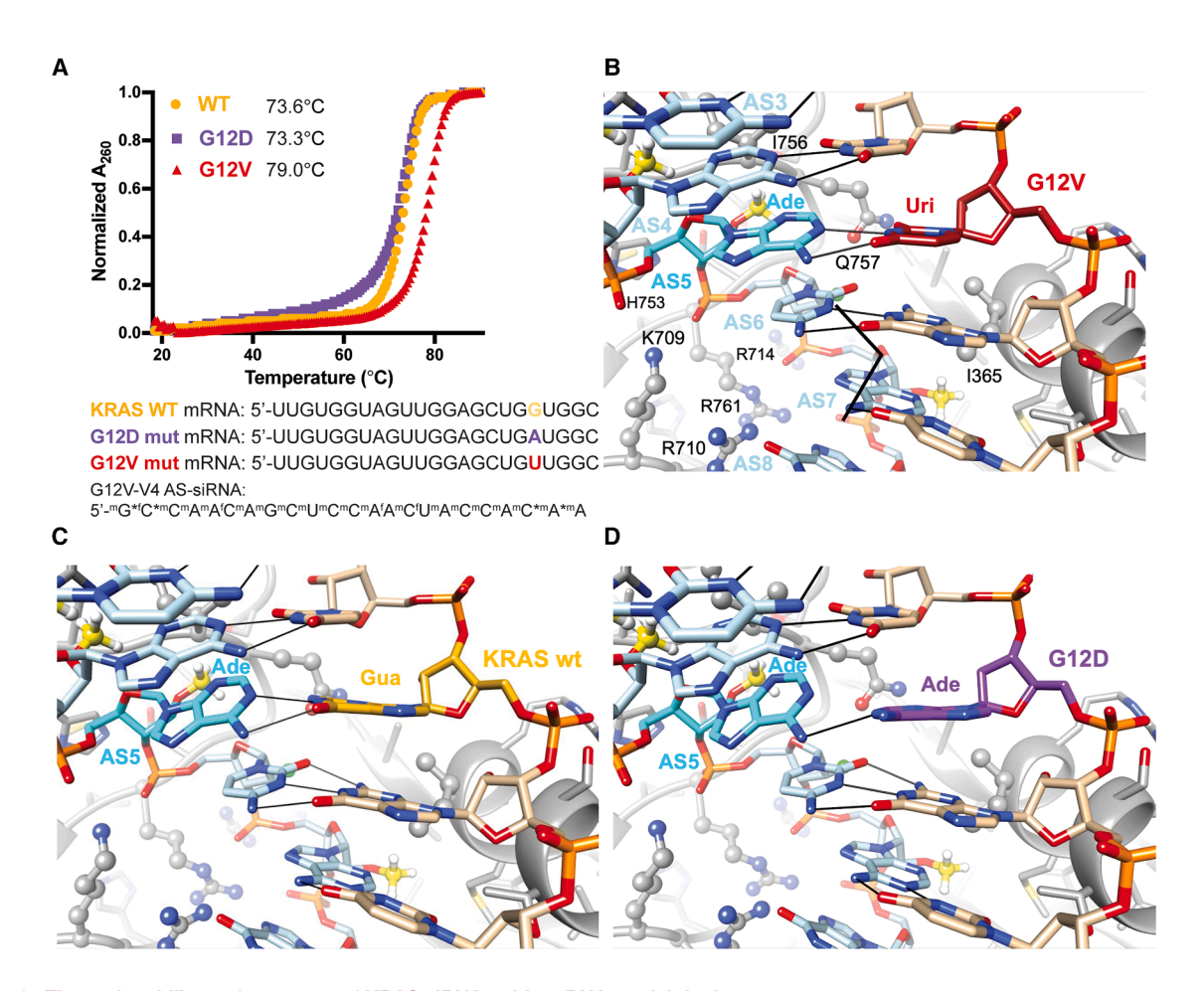


Figure 2. Thermal stability and structure of KRAS siRNA guide:mRNA model duplexes

(A) UV melting curves and sequences of 23mer duplexes between the fully modified KRAS guide RNA and the targeted *G12V* mutant, *WT*, and *G12D* mutant RNA. Molecular mechanics models of Ago2 in complex with the modified KRAS guide sequence paired opposite (B) *G12V* mRNA, (C) *WT* mRNA and (D) *G12D* mRNA. The views are into the major groove of the seed region and selected residues are labeled in (B). See methods for more details.

demonstration of siRNA delivery.<sup>31–33</sup> By adding a C-terminal cysteine to GE11 (hence GE11C), we used a PEG3 linker to conjugate the ligand to the 3′-end of the sense strand of the G12V siRNA, henceforth referred to as EFTX-G12V (Figure 3C).

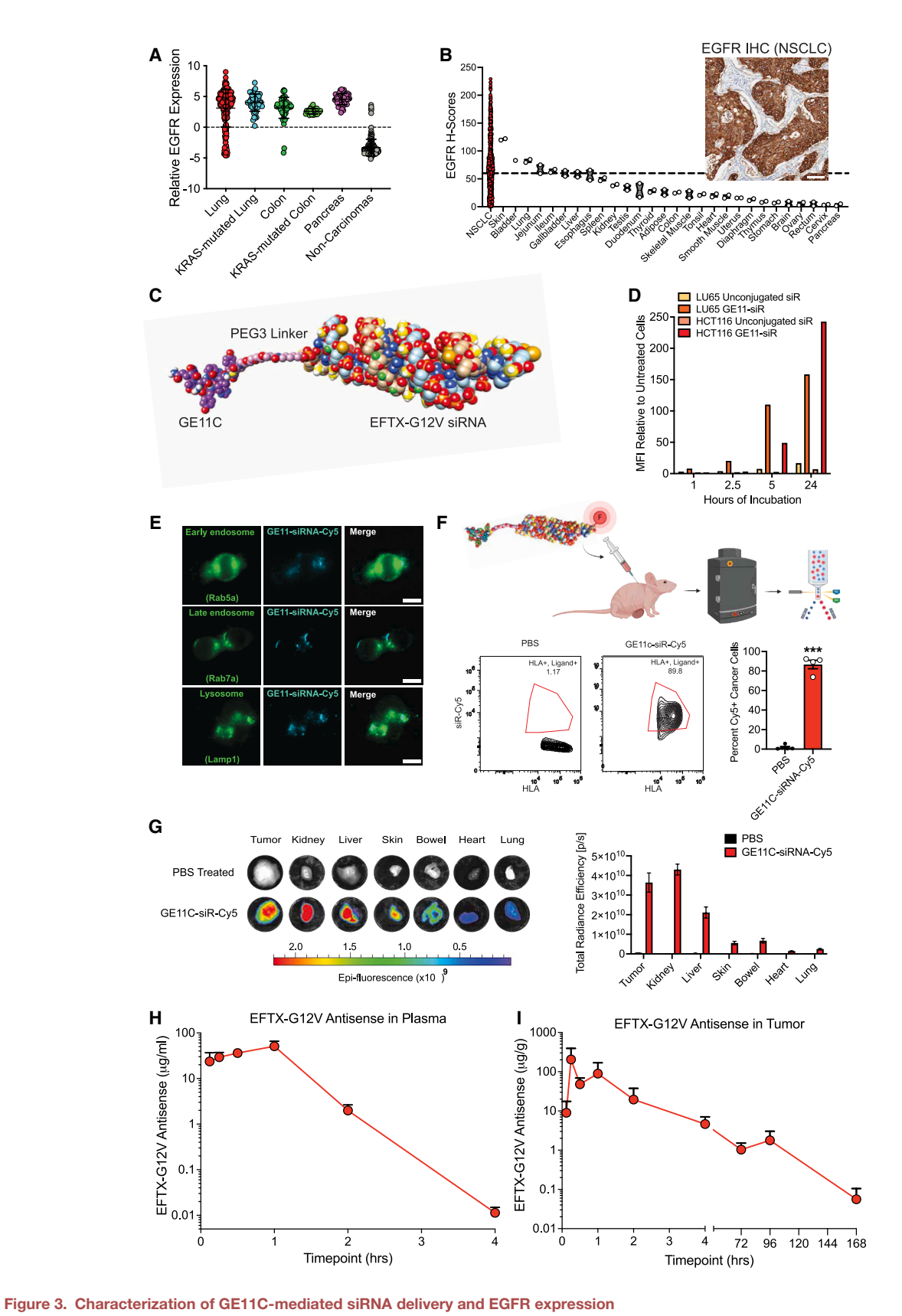
We found that compared with unconjugated Cy5-siRNAs, GE11C-conjugated Cy5-siRNAs showed a dramatic increase in uptake by 5 h (15-fold in LU65 and 17-fold in HCT116) (Figure 3D), demonstrating delivery of chemically modified siRNAs to EGFR expressing cancer cells. One potential advantage of GE11 for tumor targeted siRNA delivery is its relatively weak binding affinity to EGFR, which has been shown to allow receptor recycling to the cell surface within  $\sim$ 30 min, as opposed to a more potent binder which increases susceptibility for proteosome degradation.<sup>34</sup> To determine if GE11C-mediated siRNA delivery occurs via receptor-mediated endocytosis, we performed co-localization studies with GE11C-conjugated Cy5pan-KRAS siRNAs and markers for endosomal compartments. GE11C-conjugated siRNAs co-localized with markers for early (Rab5a) and late endosomes (Rab7a), and early-stage lysosomes (Lamp1) (Figure 3E).

We evaluated the properties of GE11C-siRNA via SQ administration  $^{21,35}$  in the A431 human xenograft model. Two hours

following a single injection (5mg/kg, mpk), compared to PBS controls, FACS sorting and analysis showed that  $\sim\!\!90\%$  of cancer cells were positive for the Cy5-siRNA (Figure 3F). This was confirmed spatially using fluorescence microscopy (Figure S3B). Using ex~vivo biofluorescence, we evaluated Cy5-siRNA uptake in tumor and in somatic tissues we found to have elevated EGFR expression (Figure 3B). When normalized by tissue mass, we observed significant tumor and kidney uptake, consistent with the class effect of ligand-conjugated siRNAs. Additionally, we observed significant uptake into mouse skin, liver and small bowel, but minimal uptake into the heart and lung (Figure 3G). Considering the tissues evaluated, tumor uptake represented 6% of the recovered dose, which is favorable controlled to the estimated  $\sim\!\!1\%$  of tumor uptake from monoclonal antibody distribution.  $^{36}$ 

Lastly, we performed a pharmacokinetic evaluation of the antisense strand of EFTX-G12V in plasma and A431 tumors following a single 5 mpk SQ injection. As anticipated for ligand-conjugated siRNAs, plasma siRNA concentration was high early and reached a peak concentration one hour after injection and was cleared within four hours (Figure 3H). In the tumor, siRNA abundance peaked between 15 min and one hour post





(A) Quantification of cell surface EGFR expression levels in cancer tissues vs. *KRAS*-mutated cancer tissues. Data were derived from the Cancer Cell Line Encyclopedia (CCLE).



injection and slowly decreased over 96 h until it was almost fully cleared one week after injection (Figure 3I). Taken together, these data indicate that EFTX-G12V is efficiently delivered to the tumor's cancer cells and somatic tissues that express EGFR and is predominately cleared from the plasma via the kidneys.

#### Pharmacodynamics, biodistribution, and safety

To characterize the pharmacodynamics of EFTX-G12V, we utilized the A431-KRAS G12V-HA tagged cell line model. This allowed us to evaluate direct *KRAS*<sup>G12V</sup> target engagement within tumor cells and distinguish the effects from the murine stroma. PBS was used as a control, and we have found that KRAS mRNA and protein expression are not differentially affected by treatment with PBS, or GE11C-conjugates to a non-targeting control siRNA (control siR1) or a luciferase targeting siRNA with the same 2'F/2'OMe modification pattern as EFTX-G12V (control siR2) (Figures S4A and S4B).

Compared to mice treated with PBS, we observed a significant time- and dose-dependent reduction in KRAS<sup>G12V</sup> and phosphorylated ERK1/2<sup>T202/Y204</sup> (Figure 4A). We observed peak reduction of KRAS at 72 h in the 2.5 mpk group (65%, Figure 4B) and at 48 h in the 5 mpk group (80%, Figure 4B). In the 2.5 and 5 mpk groups, KRAS protein expression rebounded to levels close to baseline by 96 h. In the 10 mpk group, we observed significant inhibition of KRAS protein at all timepoints, with peak KRAS silencing at 96 h (85%, Figure 4B).

We observed significant reduction of downstream signaling as evidence by reduction of phosphorylated ERK1/2<sup>T202/Y204</sup>. In the 2.5 mpk group, pERKT202/Y204 expression decreased over time and reached peak silencing at 96 h (78%). In the 5 and 10 mpk groups, pERK<sup>T202/Y204</sup> expression was significantly reduced across all timepoints assessed, reaching peak silencing  $(\sim 80\%)$  by 24 h and maintaining sustained silencing through 96 h (Figure 4C). We additionally assessed DUSP6 mRNA as a readout of ERK1/2 transcriptional activity. In the 2.5 mpk group, DUSP6 expression closely mirrored pERK1/2Y202/T204 expression, displaying a decrease over time with peak silencing at 96 h (74%). Additionally, in the 5 and 10 mpk groups, DUSP6 was significantly reduced at nearly all timepoints, with peak silencing at 96 h (91%) and 72 h (91%), respectively (Figure 4D). Lastly, to evaluate whether EFTX-G12V can spatially attenuate MAPK signaling throughout the tumor, we performed immunohistochemistry for pERK. Compared with PBS treated tumors, EFTX-G12V significantly attenuated pERK signaling at all doses and timepoints (Figures 4E and S4C). These findings corroborate the western blot findings and provide evidence for diffuse tumor distribution and effective RNAi activity for up to 4 days after a single treatment.

Next, we measured *KRAS* mRNA expression in the tumor and observed significant reductions in nearly all conditions, with peak silencing at 72 h in the 2.5 (75%) and 10 mpk (79%) groups, or at 96 h in the 5 mpk (87%) group (Figure 4F). We quantified the concentration ( $\mu$ g/g) of the antisense strand of EFTX-G12V delivered to the tumor and found a dose-dependent increase in siRNA abundance (Figure 4G). Further, we found that EFTX-G12V antisense concentration in the tumor was significantly correlated with KRAS protein silencing at the 48-h timepoint, consistent with delivery and distribution of EFTX-G12V throughout the tumor and cytosolic bioavailability for target engagement (Figure 4H).

Given the biodistribution profile of GE11C-siRNA into kidney, bladder and skin, we next analyzed murine *KRAS* expression. Because EFTX-G12V binds to a region of the *KRAS*<sup>WT</sup> mRNA sequence that is conserved between humans and mice, this enabled us to probe *in vivo* whether EFTX-G12V can inhibit *KRAS*<sup>WT</sup>. In the kidney and bladder tissues, we observed a modest, but insignificant, reduction of *KRAS* mRNA in a few of the experimental groups (Figures 4I and 4J). We did observe high concentrations of the siRNA in the kidney, particularly in the 5 mpk and 10 mpk groups at 24 h, which was quickly cleared (Figure S4D). We also observed a statistically significant but moderate reduction of *KRAS* mRNA in the skin tissue (Figure 4K). While much of our previous data shows that EFTX-G12V has excellent mutant selectivity, further longer-term safety studies will be important to better understand these findings.

Next, we performed a preliminary safety study of EFTX-G12V in C57/B6J immunocompetent mice. We observed no changes in animal behavior, total weight, organ weight, bone marrow, and liver or kidney function. Additionally, based on the white blood cell differential, there was no evidence of an inflammatory response (Figures S5A and S5G). Using miRNAscope technology, a custom probe against the EFTX-G12V AS strand confirmed systemic biodistribution, which predominately accumulated based on vascular delivery and EGFR expression, notably to the skin, kidney, liver, and bladder wall (Figure S6). Histologic examination found that the renal cortex had mild cytoplasmic basophilia in the proximal tubules in the 50 mpk group (Figure S5H). Minimal vacuolation of the proximal tubular cytoplasm was evident at all treatment doses; however, there was no evidence of microscopic deficits (Table S1). No test article related microscopic findings were evident in the tissues examined. Based on these findings, we determined EFTX-G12V likely has a large therapeutic index, consistent with several tiers of selectivity through EGFR-based targeting and KRAS<sup>G12V</sup> mutant selectivity.

<sup>(</sup>B) EGFR H-scores for NSCLC vs. normal somatic tissues derived from a tissue microarray. Inset shows a representative micrograph of EGFR IHC signal in NSCLC, scale bar 100 μM.

<sup>(</sup>C) Space-filling illustration of the 3D model of the chemically modified G12V siRNA duplex with the conjugated GE11C EGFR peptide ligand. Peptide ligand and antisense strand 3'-terminal overhanging nucleotides are shown on the upper left and lower right, respectively. See methods for more detail.

<sup>(</sup>D) Quantification of GE11C-mediated fluorescent siRNA uptake via flow cytometry.

<sup>(</sup>E) Fluorescent micrographs showing co-localization of GE11C-conjugated cy5 siRNA with endosomal and lysosomal markers, scale bar 10 µm.

<sup>(</sup>F) Cartoon showing GE11C-conjugated cy5 siRNA (top panel). FACS (left panel) and micrograph (right panel) quantification of GE11C-conjugated cy5 siRNA uptake in HLA+ cancer cells (left panel).

<sup>(</sup>G) Ex vivo quantification of GE11C-conjugated cy5 siRNA uptake tumors and mouse somatic tissues.

<sup>(</sup>H) Quantification of EFTX-G12V antisense strand in plasma and (I) tumor. All data are shown as a mean ± S.E.M. Statistical significance was measured using Student's t test; p-values \*\*\*p=<0.005. See also Figure S2.



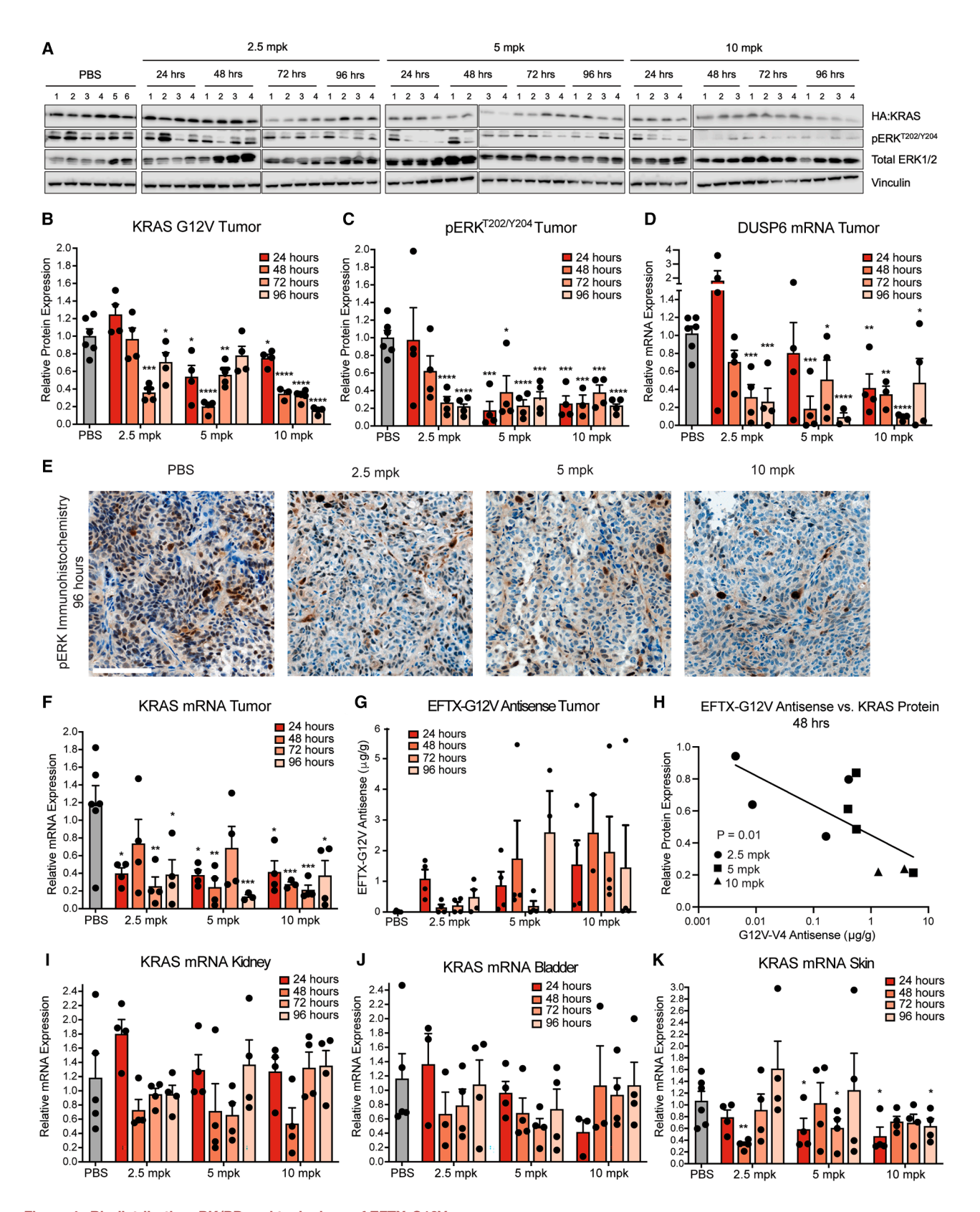


Figure 4. Biodistribution, PK/PD and toxicology of EFTX-G12V

(A) Western blot analysis in tumor lysates. Blots were done separately, and quantification is based on vinculin control for each individual blot. Representative vinculin blot shown. Separate blots are indicated and additionally separated by dosing group for clarity.



#### **EFTX-G12V** efficacy compared with pan-KRAS siRNAs

We next evaluated EFTX-G12V for its single-agent therapeutic efficacy in mouse xenograft models. To evaluate generalizable populations of *KRAS*-mutant carcinomas, we chose *KRAS*<sup>G12V</sup> models from lung carcinoma, H727 and H441, colon carcinoma, SKCO1, and pancreatic adenocarcinoma (PDAC), Capan-2, based on them each having average levels of EGFR expression for carcinoma cell lines (Figures 3A and 5A). We confirmed by IHC that these models have EGFR H-score ranges (H727: 57, H441: 155, SKCO1: 79), which may enable discrimination of tumor-to-normal tissue payload delivery.

In H727, we unexpectedly found that compared to the control siRNA, EFTX-G12V outperformed pan-KRAS targeting, despite the latter being significantly more potent in vitro (Figure 5B). At day 7, we observed significant inhibition of tumor growth in the pan-KRAS (47%) and EFTX-G12V (68%) groups. By day 21, the differences were more pronounced, and tumor growth was significantly inhibited in the pan-KRAS (60%) and in the EFTX-G12V (82%) group. When repeated in H441, pan-KRAS targeting had no effect, whereas EFTX-G12V inhibited tumor growth by 73% (Figure 5C). Next, using SKCO1, we added a treatment group of EFTX-G12V at 5 mpk once per week to assess whether we could decrease the dosing frequency of EFTX-G12V while maintaining efficacy. We found that EFTX-G12V dosed once per week decreased overall tumor growth at the same level as pan-KRAS dosed twice weekly. However, EFTX-G12V administered twice per week showed the highest efficacy (Figure 5D). Since GE11C-conjugated siRNAs require continuous EGFR expression for effective delivery, we evaluated the longest efficacy experiment (H441 - 28 days) and found no evidence that repetitive treatments resulted in decreased EGFR expression (Figure 5E).

To better understand the differences in efficacy between pan-KRAS and EFTX-G12V targeting, we evaluated several signaling pathways in SKCO1 and H441 tumors (Figure 5F). In SKCO1 tumors, we found robust pERK<sup>T202/Y204</sup> inhibition in the EFTX-G12V group (61-84%) and inconsistent pERK<sup>T202/Y204</sup> inhibition in the pan-KRAS group. We also observed robust pEGFRY1068 inhibition in the EFTX-G12V group, whereas three of the five tumors in the pan-KRAS group had increased phosphorylated EGFR, and all five had elevated levels of total EGFR. We observed similar patterns in H441 tumors, where EFTX-G12V treatment resulted in more sustained inhibition of both  $\mathsf{pERK}^{\mathsf{T202/Y204}}$  and  $\mathsf{pEGFR}^{\mathsf{Y1068}}$  compared to pan-KRAS (Figure S7A). We compared abundance of the EFTX-G12V and pan-KRAS antisense siRNA strands in the tumor tissue and found that the siRNA accumulates similarly following multiple weeks of dosing (Figures S7B and S7C). Further, we observed robust KRAS protein silencing in tumors treated with pan-KRAS following one injection (Figure S7D). These data indicate that the differences in efficacy and signaling seen after multiweek treatments are not due to lack of delivery or KRAS silencing by the pan-KRAS siRNA. We further confirmed *in vivo KRAS* ranscript selectivity by evaluating MAPK signaling in H358 (*KRAS* <sup>G12C</sup>) tumors and did not find a change in pERK <sup>T202</sup>/Y<sup>204</sup> (Figure S7E).

We next probed the SKCO1 tumors for phosphorylation of YAP at S127 and Y357, which are markers of YAP activation following canonical Hippo signaling and non-canonical FAK/Src signaling, respectively. <sup>37,38</sup> We observed a robust reduction in pYAP s127 in four of six tumors of the EFTX-G12V group (55–82%) and a moderate reduction in two of five tumors of the pan-KRAS group (14–41%), and inconsistent changes in phosphorylation of YAP s1357 in both groups. These data indicate potential nuclear translocation of YAP and canonical activation of YAP transcriptional activity in EFTX-G12V treated tumors. Activation of YAP signaling has emerged as a resistance mechanism for KRAS inhibitors, and our findings merit additional studies to understand YAP signaling following treatment with EFTX-G12V. <sup>39–42</sup>

Further, our data indicate potential reactivation of both MAPK signaling and RTK signaling via EGFR in the pan-KRAS group and sustained pathway inhibition in the EFTX-G12V group, which in part may explain the enhanced efficacy in the latter. Additionally, we found that in cells transfected *in vitro* and assayed over a short time course, pEGFR<sup>Y1068</sup> was generally not reactivated by pan-KRAS or KRAS<sup>G12V</sup> silencing, indicating that differences seen *in vivo* are likely occurring following multi-week treatment, and may in part be attributable to non-cell autonomous effects (Figures S8A and S8C).

Based on our findings in the SKCO1 colon tumors regarding RTK reactivation via EGFR, we evaluated whether EFTX-G12V could be combined with cetuximab, an anti-EGFR targeting antibody, to improve efficacy. Compared to the control siRNA group, tumor volume was significantly reduced in both EFTX-G12V (62%) and EFTX-G12V with cetuximab (77%) groups (Figure 5G). Similar to prior observations with KRAS<sup>G12C</sup> inhibitors, the addition of cetuximab resulted in a significant increase in tumor regression (Figure 5H). A few of the EFTX-G12V treated tumors were growing on treatment, and in those tumors, both pEGFR<sup>Y1068</sup> and pERK<sup>T202/Y204</sup> were elevated compared to the control group (Figures 5H and 5I).

Lastly, we completed additional efficacy studies in H727 and Capan-2 (PDAC). In H727, by day 11, EFTX-G12V resulted in a 70% response rate from baseline, and three tumors had a complete and durable response (Figure 5J), and by 21 days, tumor growth was significantly inhibited by 78% (Figure 5K). We additionally evaluated a second control siRNA with the same modification pattern as EFTX-G12V and did not observe any differences in tumor volume between the control siRNAs (Figure S8D). In Capan-2, we observed significant tumor growth inhibition after

<sup>(</sup>B) Quantification of western blot analysis for KRAS<sup>G12V</sup> (HA) and (C) pERK<sup>T202/Y204</sup>.

<sup>(</sup>D) RT-qPCR analysis of DUSP6 mRNA in tumors, normalized to average PBS (n=6).

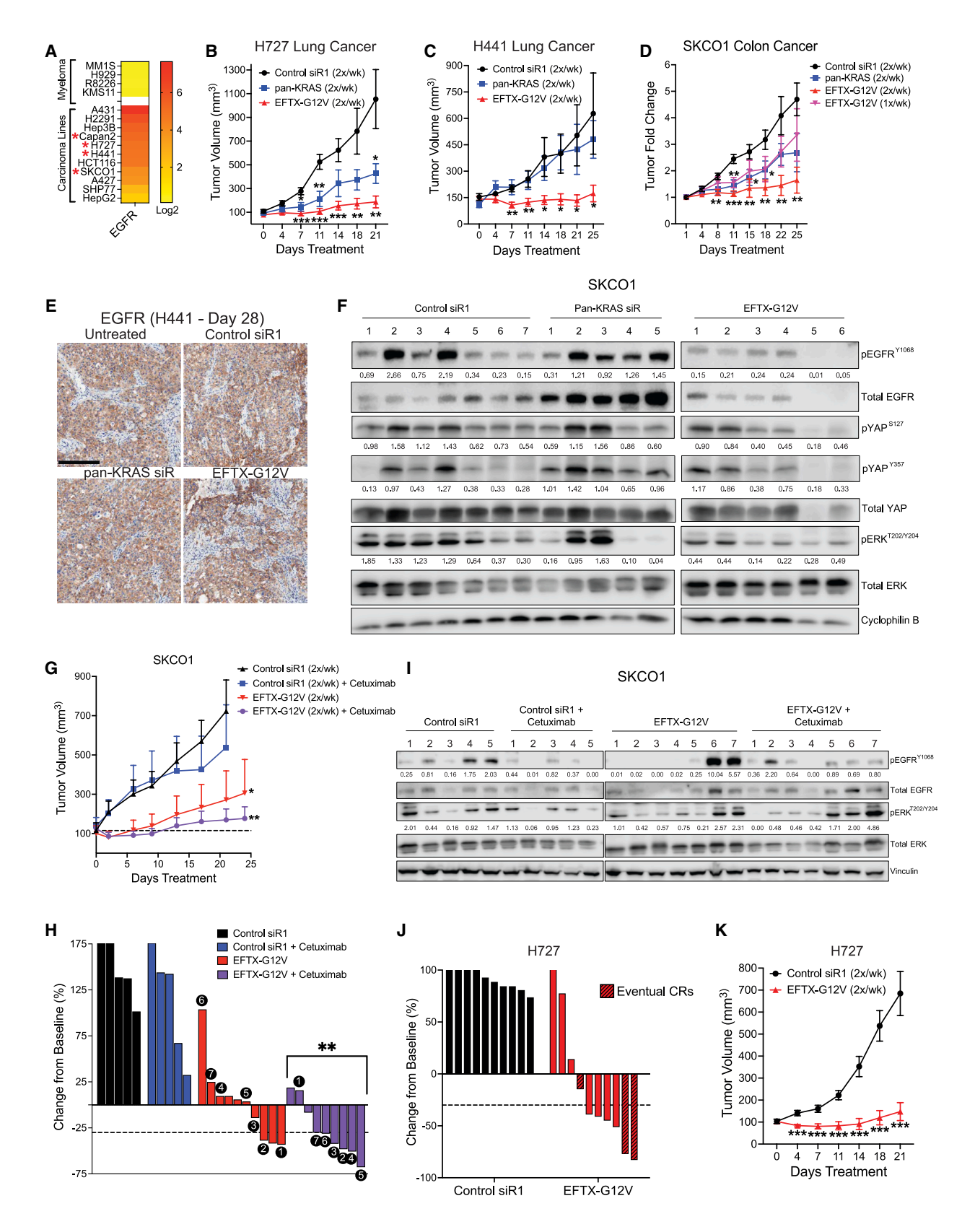
<sup>(</sup>E) Immunohistochemistry for pERK in tumors treated with PBS (24 h) or respective doses (96 h), scale bar 100 µm.

<sup>(</sup>F) RT-qPCR analysis of  $KRAS^{G12V}$  mRNA in tumors, normalized to average PBS (n = 6).

<sup>(</sup>G) Stem-loop RT-qPCR of EFTX-G12V antisense strand in tumors.

<sup>(</sup>H) Spearman correlation of EFTX-G12V antisense and KRAS protein expression at 48 h. RT-qPCR analysis of  $KRAS^{WT}$  mRNA in (I) kidney, (J) bladder, and (K) skin samples. All data shown as mean  $\pm$  S.E.M. Statistical significance was measured by one-tailed Student's t test; p-values are indicated as p < 0.05, p < 0.05,





(legend on next page)



three weeks of treatment, with a 50% reduction in tumor volume in EFTX-G12V group (Figure S8E). Based on these data from diverse *KRAS*<sup>G12V</sup> models, EFTX-G12V is highly effective at inhibiting tumor growth and consistently outperformed the pan-KRAS siRNA. These findings demonstrate proof-of-concept that an EGFR-directed *KRAS*<sup>G12V</sup> mutant-selective siRNA molecule can be sufficiently delivered with significant therapeutic efficacy.

## Efficacy of EFTX-G12V in an immunocompetent model

Next, we compared EFTX-G12V treatment with temporally controlled ablation of the KRASG12V allele in an immunocompetent lung adenocarcinoma model. Previously, genetically engineered  $Kras^{+/FSFG12Vlox}; Trp53^{F/F}; Rosa26-CreERT2^{KI/KI}; Tg.$ hUBC-CreERT2+/T (KG12VloxPC2) mice were exposed to Adeno-FLPo particles to induce lung tumors. 44 Using MPK195 cell lines obtained from KG12VIoxPC2 tumors, syngeneic tumors were established. Mice were treated with either GE11C-control siRNA, tamoxifen (to excise the conditional KRAS<sup>G12Vlox</sup> alleles), or EFTX-G12V (Figure 6A). After 3 days we observed significant tumor reductions with either tamoxifen or EFTX-G12V treatment, and by 7 days EFTX-G12V treatment resulted in half the tumors showing significant tumor regression (Figures 6B and 6C). Consistent with observations with the KG12VloxPC2 genetic model44 and a degradation tag KRAS<sup>G12V</sup>-transgenic mouse to model KRAS<sup>G12V</sup> protein degradation, 45 we observed a rapid infiltration of CD8 T cells with tamoxifen and EFTX-G12V (Figure 6D). Furthermore, consistent with a robust anti-tumor immune response, we detected elevated granzyme B expression in several tumorlocalized lymphocyte populations with tamoxifen and EFTX-G12V treatment (Figure 6E). Similar to our safety study, we observed no significant changes in white blood cell differential (Figure S9), supporting these immune TME changes are not the result of a systemic inflammatory response. Together, in the acute setting the therapeutic efficacy of EFTX-G12V can nearly phenocopy genetic ablation of KRAS<sup>G12V</sup> and is associated with rapid infiltration of anti-tumor immunity that parallels that of targeted removal of the KRAS<sup>G12V</sup> alleles or protein.<sup>44,45</sup>

#### Anti-angiogenic effects of KRAS G12V targeting

Although, we consistently found pan-KRAS siRNA is more potent at reducing KRAS expression than EFTX-G12V *in vitro* (Figure 1), the improved efficacy of EFTX-G12V over pan-KRAS siRNA *in vivo* across models led us to evaluate whether mutant-specific KRAS targeting also results in anti-tumor effects in the TME. To determine the dynamic transcriptional effects of mutant-selective versus pan-KRAS targeting, we performed RNA-sequencing in H441 and H727 cells. Similar to our findings in the SKCO1 cell

line (Figure 1H), for both cell lines the mutant-selective silencing resulted in fewer differentially expressed genes than pan-KRAS silencing (Figure 7A). Consistent with known roles of mutant KRAS targeting, pre-ranked gene set enrichment analyses (GSEA-PR) demonstrated EFTX-G12V led to significant suppression of pathways associated with MAPK signaling, MYC activation and translational initiation (Figures 7B; Tables S2 and S3).

We observed several transcriptional programs more significantly suppressed with EFTX-G12V than pan-KRAS siRNA (Tables S4 and S5), including several cancer hallmark pathways such as epithelial-mesenchymal transition (EMT), myogenesis, TGF-β, TNFα/NF-κB, and WNT/Beta-catenin signaling (Figure 7C). Interestingly, many suppressed pathways within the TME were also observed, many of which are associated with tumor angiogenesis (Figure 7C). Furthermore, pathways associated with tumor hypoxia and VEGFa-VEGFR2 signaling were significantly suppressed with EFTX-G12V compared with control siRNA (Figures 7D-7F). Although mutant KRAS signaling is known to promote tumor angiogenesis via VEGFa and chemokine signaling, <sup>46</sup> the distinction between the effects of pan-KRAS and mutant-selective KRAS targeting on tumor angiogenesis remains poorly understood.

We evaluated micro-vessel density (MVD) in vivo in the H727, H441, and SKCO1 models after at least 2 weeks of treatment. The effects of pan-KRAS siRNA targeting on MVD were largely model dependent. In H727, we observed a significant increase in MVD (50%), but no significant differences in H441 between control and pan-KRAS siRNAs (Figures 7G and 7H). In SKCO1, pan-KRAS siRNA targeting resulted in a significant reduction in MVD (32%) (Figure 7I). However, in both lung cancer models, EFTX-G12V treatment resulted in significant reductions in MVD compared with control siRNA (H727: 28%, H441: 37%) (Figures 7G and 7H). Consistent with the therapeutic effects observed with EFTX-G12V versus pan-KRAS siRNA in SKCO1, and when comparing once versus twice weekly EFTX-G12V dosing, we observed correspondingly significant MVD reductions (1x/wk: 48%, 2x/wk: 59%) (Figure 7I). These differences in tumor angiogenesis effects observed between pan-KRAS and mutant-selective targeting were largely concordant with the observed efficacy in each model. Taken together, our findings reveal mutant-selective KRASG12V silencing may have several therapeutic advantages over a pan-KRAS approach, including potent inhibition of tumor angiogenesis.

### **DISCUSSION**

Activating mutations in KRAS are among the most common oncogenic drivers in cancer and pose a tremendous public

#### Figure 5. Efficacy of GE11C-conjugated EFTX-G12V siRNA in lung and colon xenograft models

(A) Heatmap showing EGFR expression in non-carcinoma (myeloma) and carcinoma cell lines (\* indicates the cell lines used in this study). Data was derived from the Cancer Cell Line Encyclopedia (CCLE). Average xenograft tumor volume in athymic mice treated with 5 mpk of GE11C-siRNAs in (B) H727 (n = 10), (C) H441 (n = 6-9 per group) and (D) SKCO1 (n = 8).

- (E) EGFR IHC for H441 xenograft tumors, scale bar 50 µm. (F) Western blot analysis in SKCO1 tumors. Quantification based on cyclophilin B.
- (G) Average xenograft tumor volume in mice treated with 5 mpk GE11C-control siRNA (n = 5), 50 mpk cetuximab (n = 5), EFTX-G12V (n = 9) or combination (n = 9).
- (H) Waterfall plot of tumor change from baseline after 7 days of treatment. Tumor numbers shown correlate with western blot.
- (I) Western blot analysis in tumors, lanes indicated by tumors from waterfall plot in panel J. Quantification based on vinculin.
- (J) Waterfall plot of tumor change from baseline after 14 days of treatment (5 mpk). Complete Responses (CR) after treatment shown as hatched bars.
- (K) Average tumor volume in mice treated with 5 mpk dose of GE11C-siRNAs (n = 10). Statistical significance was measured by one-way ANOVA; p-values are indicated as \*p < 0.05, \*\*p < 0.01, \*\*\*p < 0.005, \*\*\*p < 0.001. See also Figure S6.



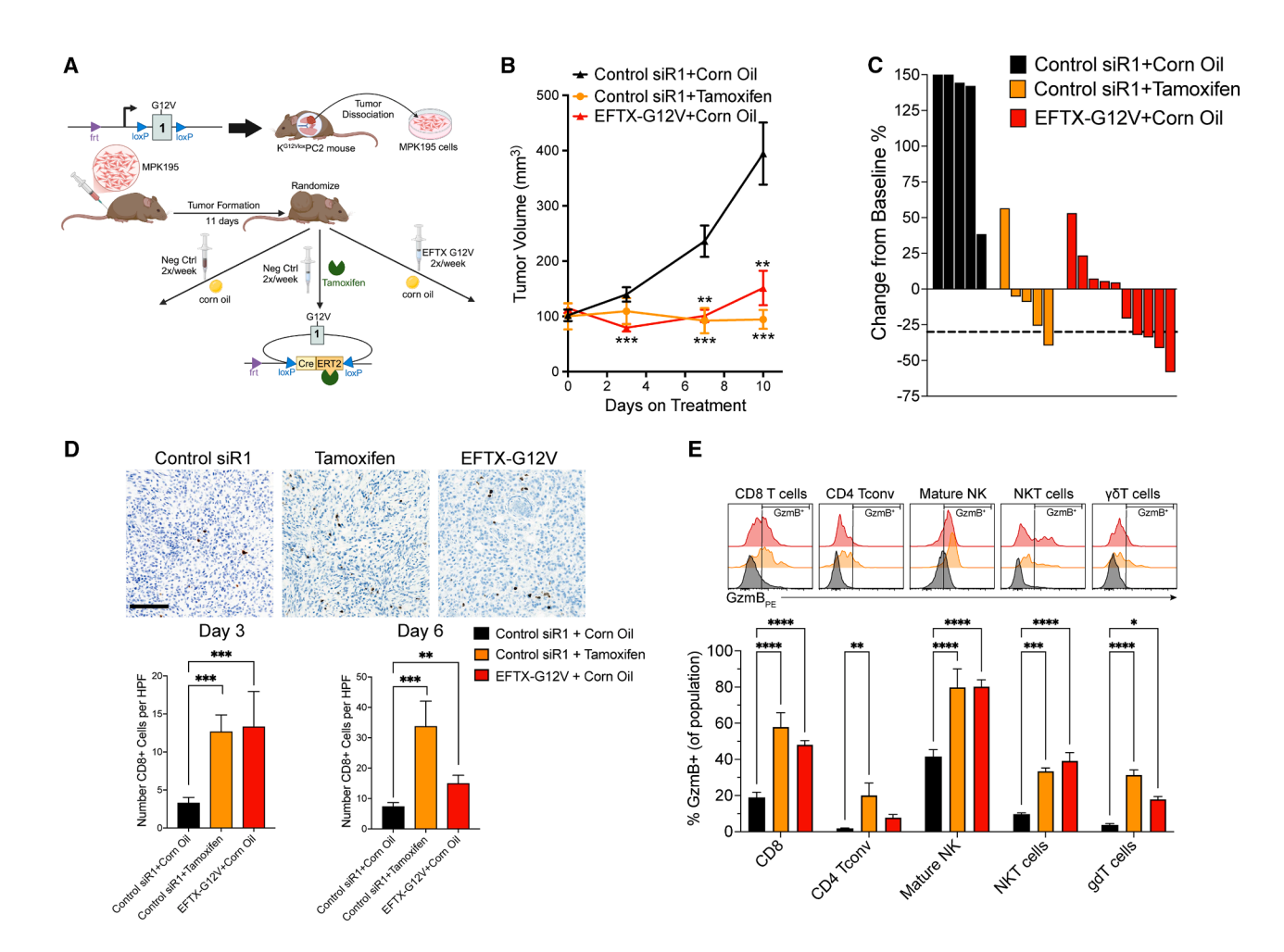


Figure 6. Efficacy of GE11C-conjugated EFTX-G12V siRNA in immunocompetent model

- (A) Schematic of derivation of MPK195 cells from a K<sup>G12Vlox</sup>PC2 inducible knockout mouse model and experimental procedure in immunocompetent mice.
- (B) Average MPK195 xenograft tumor volume in mice treated with control siR + corn oil (n = 5), control siR + tamoxifen (n = 5) or EFTX-G12V + corn oil (n = 10). (C) Waterfall plot of tumor change from baseline after 7 days treatment.
- (D) Representative CD8a IHC images from tumors obtained at Day 3, scale bar 100 μm. Quantification of CD8a+ cells per high power field at 3 and 6 days of treatment.

(E) Spectral flow cytometry of granzyme B+ adaptive immune cells at 6 days following treatment. Statistical significance was measured by two-tailed Student's t test or a two-sided ANOVA multiple comparisons test; p-values are indicated as p < 0.05, p < 0.01, p < 0.005, p < 0.001. See also Figure S7.

health concern. The recent development of effective KRAS inhibitors has resulted in a surge in excitement in the field, however, numerous obstacles remain. Numerous mechanisms of resistance have been described, including secondary mutations in *KRAS* and/or mediators of MAPK signaling,<sup>47–49</sup> feedback activation of parallel pathways,<sup>50</sup> YAP/TAZ activation,<sup>51</sup> amplification of *KRAS* or *MYC*,<sup>13,44</sup> remodeling of the TME, and immune escape.<sup>52</sup>

Recently, temporally controlled genetically engineered mouse models (GEMMs) of lung adenocarcinoma demonstrated that genetic ablation of either  $KRAS^{G12V}$  or  $KRAS^{G12C}$  alleles was sufficient to induce  $\sim\!100\%$  complete responses in autochthonous tumors. However, use of sotorasib (KRAS G12C) only resulted in a 23% complete response rate, and rapid emergence of KRAS amplifications was detected in resistant tumors. Interestingly, treatment interruptions with sotorasib resulted in fewer KRAS amplifications and resensitized tumors to the drug,  $^{44}$  a

treatment strategy recently postulated using simple mathematical models. These findings suggest that resistance to KRAS inhibitors could be prevented if more pronounced inhibition of KRAS signaling could be achieved, similar to genetic *KRAS* ablation. Whether more potent KRAS inhibitors, or a combination of modalities that target KRAS at multiple levels (e.g., small molecule inhibitors plus protein degraders or RNAi strategies) will result in more robust clinical responses remains unclear. 5,6

Most KRAS inhibitors in development depend on binding to the "OFF" GDP-bound state. However, because  $KRAS^{G12V}$  mutations have one of the slowest intrinsic hydrolysis rates compared to more rapid cyclers, the KRAS G12V GDP-bound state is a less frequently available substrate, making for a more challenging target for small molecule inhibitors. Also To address the significant unmet need for a KRAS G12V selective inhibitor, we developed EFTX-G12V, a ligand-conjugated, fully chemically modified, mutant-specific siRNA.



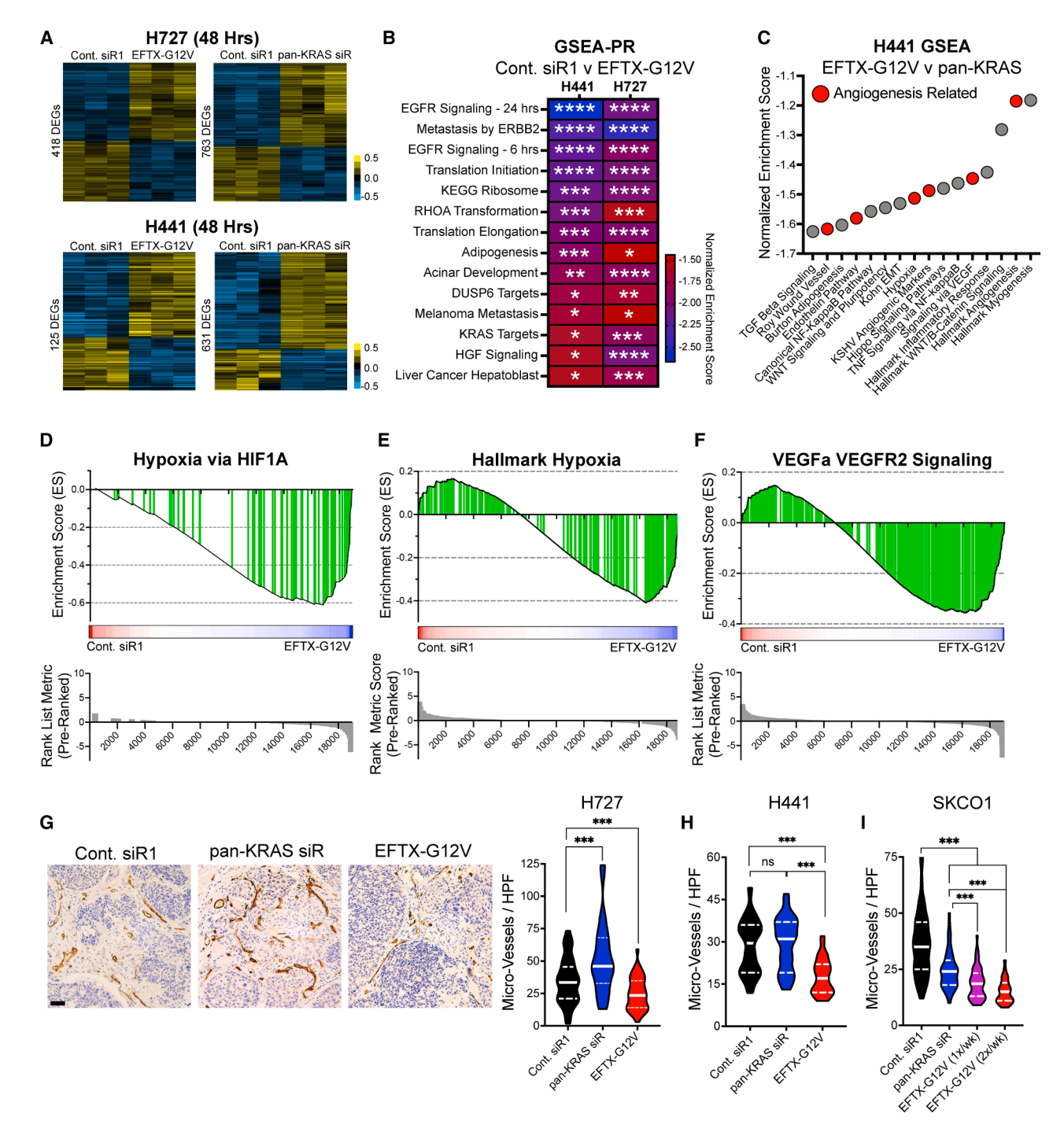


Figure 7. Selective KRAS G12V Silencing Inhibits Cancer Hallmarks and Tumor Angiogenesis

(A) Heat maps of differentially expressed genes in cells transfected with 20 nM siRNA.

(B) Pre-ranked Gene Set Enrichment Analysis (GSEA-PR) results. Normalized enrichment score and significance indicated for selected pathways. Adjusted false discovery rate (FDR) values are as follows: \*FDR<0.25, \*\*FDR<0.1, \*\*\*FDR<0.05, \*\*\*\*FDR<0.01.

(C) GSEA-PR results of H441 pan-KRAS versus EFTX-G12V showing normalized enrichment scores. Pathways associated with angiogenesis shown in red. (D) Enrichment plots from GSEA-PR in H727 cells comparing control siRNA to EFTX-G12V. Pathways selected are involved in angiogenesis including hypoxia via HIF1A, (E) hallmark hypoxia, and (F) VEGFa-VEGFR2 signaling.

(G) Representative IHC for CD31 and quantitative micro-vessel density (MVD) for H727, scale bar, 50 µm. Tumors were collected 14 days following treatment with siRNAs (5 mpk, twice weekly). MVD was calculated as micro-vessels per higher-power field (HPF).

(H) MVD quantification for H441 (collected day 28) following treatment with siRNAs (5 mpk, twice weekly).

(I) MVD in SKCO1 treated with siRNAs, (5 mpk). Statistical significance was measured by two-tailed Student's t test; p-values are indicated as \*p < 0.05, \*\*\*p < 0.01, \*\*\*p < 0.005, \*\*\*p < 0.001.



Given the success of GalNAc-conjugated siRNAs for ASGPRmediated liver targeting, ligand conjugation has garnered attention as a potential solution for extrahepatic diseases such as cancer. However, there is a critical need to identify specific tumor-targeting moieties. We confirmed that EGFR is highly expressed in KRAS mutant cancers, and to a lesser extent in normal tissues such as skin, bowel, and bladder. We utilized a previously described EGFR ligand, GE11, which does not activate EGFR signaling,<sup>31</sup> and is rapidly internalized upon binding, enabling targeted tumor delivery of siRNA payloads. Following a structure-activity-relationship screening campaign using fully chemically modified siRNAs, we identified a highly KRAS<sup>G12V</sup> selective siRNA with no apparent off-target effects. After a single dose of EFTX-G12V *in vivo*, phosphorylation of ERK1/2<sup>Y202/T204</sup> as well as DUSP6 mRNA levels were significantly reduced by  $\sim$ 80–90%, and inhibition was sustained for up to 96 h.

We observed significant single agent efficacy in lung, colon and pancreatic cancer  $KRAS^{G12V}$  models, including durable complete responses. Although we observed significant clearance of EFTX-G12V in the kidneys (a class effect of ligand-conjugated siRNAs) and uptake in high EGFR-expressing tissues, there were minimal concerning reductions in KRAS expression in these tissues, consistent with a mutant-selective design. Furthermore, in preliminary studies using immunocompetent mice, we did not observe evidence of toxicity.

In addition to an increased therapeutic window anticipated with mutant-selective targeting, we also found that EFTX-G12V had improved therapeutic efficacy in vivo compared with a pan-KRAS RNAi approach. These findings suggest that  $\mathsf{KRAS}^{\mathsf{WT}}$ may have anti-tumor effects and pan-KRAS approaches may limit efficacy in some contexts. Tumor suppressor roles for KRASWT in tumors harboring activating KRAS mutations have been previously described. 14 Loss of the KRASWT allele through genetic mechanisms in GEMMs and clinical samples of KRAS mutant disease has been implicated as a common mechanism of disease progression and metastasis.<sup>56</sup> In pancreatic cancer. KRASWT was found to prevent disease progression through HIPPO-mediated phosphorylation of YAP1S127, thereby suppressing activated YAP1 trafficking to the nucleus.<sup>57</sup> Also, genetic deletion of the KRASWT allele in a KRASG12D mutant colon cancer model rapidly accelerated MAPK signaling, intestinal proliferation and potentiated tumor initiation.<sup>58</sup> In this latter study, loss of the KRASWT allele resulted in robust activation of WNT/ Beta-Catenin signaling,<sup>58</sup> consistent with our GSEA analyses showing EFTX-G12V suppressed this pathway compared with pan-KRAS siRNA targeting. We observed that pan-KRAS siRNA targeting more often resulted in EGFR signaling than EFTX-G12V, likely contributing to pERK reactivation. Furthermore, our findings that EFTX-G12V significantly inhibited tumor angiogenesis, while pan-KRAS siRNA targeting had inconsistent angiogenic effects, further suggest that mutant-selective targeting has advantages within the TME specifically related to angiogenesis.

#### **Limitations of the study**

Our development of EFTX-G12V represents a technological advancement in cancer-based RNAi therapeutics and may hold promise for a large patient population in critical need of new therapeutic options. However, our study does have limitations, and there may be opportunities to realize the full potential

of EFTX-G12V. First, EFTX-G12V does not contain mechanisms to enhance an endosomal release, however, there are many such efforts to improve RNAi activity in cancer, and thus the potential to enhance depth and duration of target engagement is likely yet to be fully realized. 59,60 Second, the EGFR-targeting ligand (GE11) has weak affinity for EGFR, and whether more potent ligand binders result in improved cancer delivery of siRNAs remains an open question in the field. Third, we used xenograft and GEMM-derived syngeneic model systems, which may not fully predict activity of an RNAi therapeutic in cancer patients. Finally, while EFTX-G12V has demonstrated significant therapeutic effect thus far as a single agent, combination approaches may be necessary to further enhance its potential efficacy in the clinic. Our data show improved inhibition of MAPK signaling in cells treated with both EFTX-G12V and RMC-7977, suggesting that targeting KRAS at both the mRNA and protein levels with multiple therapeutic modalities may result in improved target inhibition and efficacy. Furthermore, we found that the combination of EFTX-G12V and cetuximab in a colon cancer model in vivo improved the depth and duration of response. As new mechanisms of resistance to KRAS inhibition emerge, evaluation of EFTX-G12V with combination strategies will be critical to fully appreciate the broad clinical utility of this modality.

#### **RESOURCE AVAILABILITY**

#### **Lead contact**

Requests for resources and reagents should be directed to and will be fulfilled by Chad V. Pecot (pecot@email.unc.edu).

#### Materials availability

All data generated or analyzed during this study are included in this published article (and its supplementary information files). Any unique biological materials are available upon request.

### Data and code availability

- RNA-sequencing datasets have been deposited at the Gene Expression Omnibus (GEO) as GSE278018, GSE278019 and GSE278020.
- Original western blot images have been deposited at Mendeley (DOI) as https://doi.org/10.17632/sbb397pkvc.1. Microscopy data reported in this paper will be shared by the lead contact upon request.
- This paper does not report original code.
- Any additional information required to reanalyze the data reported in this
  paper is available from the lead contact upon request.

### **ACKNOWLEDGMENTS**

C.V.P. was supported in part by the National Institutes of Health R01CA215075, 1R01CA279532, 1R41CA246848, and 1R44-CA284932, a UCRF Innovator Award, Kickstarter Venture Services Commercialization awards, Lung Cancer Initiative of North Carolina Innovation and Alumni Awards, and a North Carolina Biotechnology Translation Research Grant (NCBC TRG). Y.S.C. was supported by a T32, a UCRF Innovator Award, and a Lung Cancer Initiative of North Carolina Alumni Award. H.P.H. was supported in part by an NIH 1R41CA246848 award. S.H.A. was supported by the Duke Hematology & Transfusion Medicine Training Program (T32 HL007057), the Duke Cancer Institute Cancer Research Young Investigator Pilot Award (part of the Cancer Center Support Grant, P30 CA014236), and the American Society of Clinical Oncology Conquer Cancer Young Investigator Award supported by the Breast Cancer Research Foundation. We thank Yongjuan Xia in the Pathology Services Core for expert technical assistance with



Histopathology. The PSC is supported in part by an NCI Center Core Support Grant (P30CA016086). We also thank SynOligo and Avecia for helpful discussions with conjugation strategies and oligonucleotide synthesis. Genomics project management was performed by the Lineberger Office of Genomics Research (OGR) at the University of North Carolina-Chapel Hill, which is supported in part by the Lineberger University Cancer Research Fund, by the NIH NCI 5UG1CA233333 grant, and The UNC Center for Environmental Health and Susceptibility P30ES010126 grant. mRNA library construction and sequencing were performed by the Lineberger Translational Genomics Lab (TGL) (RRID: SCR\_025231), which is supported by the Lineberger University Cancer Research Fund. Finally, we acknowledge the UNC Lineberger Bioinformatics Core for providing the computational resources and workflow used for the RNA-seq data processing.

#### **AUTHOR CONTRIBUTIONS**

Conception and design: C.V.P.; development of methodology: H.P.H., L.J.S., Y.S.C., S.S.S., A.P., S.H.A., J.L.P., P.S.P., L.E., M.C.F., C.G.-F., V.J., G.D.L.C., A.W., M.E., A.A.B., and C.V.P.; acquisition of data (provided animals, performed experiments, provided facilities, etc.): H.P.H., L.J.S., Y.S.C., S.S.S., A.D., W.D.G., A.P., S.H.A., J.L.P., P.S.P., L.E., M.C.F., C.G. -F., V.J., R.S.S., G.D.L.C., A.W., and C.V.P.; analysis and interpretation of data (e.g., statistical analysis, biostatistics, computational analysis): H.P.H., L.J.S., A.P., R.S.S., M. E., A.A.B., and C.V.P.; writing, review, and/or revision of the manuscript: All authors; administrative, technical, or material support (i.e., reporting or organizing data, constructing databases): H.P.H., L.J.S., A.P., and C.V.P.; study supervision: C.V.P.

#### **DECLARATION OF INTERESTS**

C.V.P., S.H.A., Y.S.C., M.C.F., A.A.B., and C.V.P. hold intellectual property interests on this work. C.V.P. is founder of EnFuego Therapeutics, Inc. and holds equity in the company. L.J.S., H.P.H., V.J., and J.I. were employees of EnFuego Therapeutics at the time of this work. S.S.S., A.P., J.L.P., P.S.P., K. W., L.E., W.D.G., C.G.F., I.S., A.D., K.I.Z., R.S.S., G.D.L.C., A.W., J.M., and M.E. declare no competing interests.

#### **STAR**\*METHODS

Detailed methods are provided in the online version of this paper and include the following:

- KEY RESOURCES TABLE
- EXPERIMENTAL MODEL AND STUDY PARTICIPANT DETAILS
  - o Cell lines and culture conditions
  - $\circ\,$  In vivo modeling and tissue processing
- METHOD DETAILS
  - o siRNA transfections
  - $_{\odot}\,$  GE11C conjugation to siRNAs
  - o Immunohistochemistry and in situ hybridization
  - o Quantitative reverse transcriptase PCR
  - Analysis of PK/PD studies using SL-RT-qPCR
  - Western blotting
  - Cell viability experiments
  - o Bliss Independence synergy evaluation
  - o Luciferase experiments
  - o 3D spheroid formation assay
  - Spectral flow cytometry
  - Pharmacokinetic and pharmacodynamic studies in tumors and tissues
  - KRAS<sup>G12V</sup> siRNA duplex and conjugation modeling
  - UV melting experiments
  - Modeling of the seed region of G12V AS-siRNA paired with G12V, wt-KRAS or G12D mRNA and bound to Argonaute2
- QUANTIFICATION AND STATISTICAL ANALYSIS
  - Bioinformatics and statistical analyses of RNA sequencing data of the SKCO1 cell line

- Bioinformatics and statistical analyses of RNA-Seq data of the H441 and H727 cell lines
- Statistical analyses

#### SUPPLEMENTAL INFORMATION

Supplemental information can be found online at https://doi.org/10.1016/j.ccell.2025.05.016.

Received: August 30, 2024 Revised: March 17, 2025 Accepted: May 26, 2025 Published: June 19, 2025

#### **REFERENCES**

- Lee, J.K., Sivakumar, S., Schrock, A.B., Madison, R., Fabrizio, D., Gjoerup, O., Ross, J.S., Frampton, G.M., Napalkov, P., Montesion, M., et al. (2022). Comprehensive pan-cancer genomic landscape of KRAS altered cancers and real-world outcomes in solid tumors. npj Precis. Oncol. 6, 91. https://doi.org/10.1038/s41698-022-00334-z.
- Scharpf, R.B., Balan, A., Ricciuti, B., Fiksel, J., Cherry, C., Wang, C., Lenoue-Newton, M.L., Rizvi, H.A., White, J.R., Baras, A.S., et al. (2022). Genomic Landscapes and Hallmarks of Mutant RAS in Human Cancers. Cancer Res. 82, 4058–4078. https://doi.org/10.1158/0008-5472.CAN-22-1731.
- Janne, P.A., Riely, G.J., Gadgeel, S.M., Heist, R.S., Ou, S.I., Pacheco, J. M., Johnson, M.L., Sabari, J.K., Leventakos, K., Yau, E., et al. (2022). Adagrasib in Non-Small-Cell Lung Cancer Harboring a KRAS(G12C) Mutation. N. Engl. J. Med. 387, 120–131. https://doi.org/10.1056/NEJMoa2204619.
- Skoulidis, F., Li, B.T., Dy, G.K., Price, T.J., Falchook, G.S., Wolf, J., Italiano, A., Schuler, M., Borghaei, H., Barlesi, F., et al. (2021). Sotorasib for Lung Cancers with KRAS p.G12C Mutation. N. Engl. J. Med. 384, 2371–2381. https://doi.org/10.1056/NEJMoa2103695.
- Punekar, S.R., Velcheti, V., Neel, B.G., and Wong, K.K. (2022). The current state of the art and future trends in RAS-targeted cancer therapies. Nat. Rev. Clin. Oncol. 19, 637–655. https://doi.org/10.1038/s41571-022-00671-9
- Hofmann, M.H., Gerlach, D., Misale, S., Petronczki, M., and Kraut, N. (2022). Expanding the Reach of Precision Oncology by Drugging All KRAS Mutants. Cancer Discov. 12, 924–937. https://doi.org/10.1158/2159-8290.CD-21-1331.
- Hallin, J., Bowcut, V., Calinisan, A., Briere, D.M., Hargis, L., Engstrom, L. D., Laguer, J., Medwid, J., Vanderpool, D., Lifset, E., et al. (2022). Anti-tu-mor efficacy of a potent and selective non-covalent KRAS(G12D) inhibitor. Nat Med 28, 2171–2182. https://doi.org/10.1038/s41591-022-02007-7.
- Zhou, C., Li, C., Luo, L., Li, X., Jia, K., He, N., Mao, S., Wang, W., Shao, C., Liu, X., et al. (2024). Anti-tumor efficacy of HRS-4642 and its potential combination with proteasome inhibition in KRAS G12D-mutant cancer. Cancer Cell 42, 1286–1300.e8. https://doi.org/10.1016/j.ccell.2024.
- Zheng, Q., Zhang, Z., Guiley, K.Z., and Shokat, K.M. (2024). Strain-release alkylation of Asp12 enables mutant selective targeting of K-Ras-G12D. Nat. Chem. Biol. 20, 1114–1122. https://doi.org/10.1038/s41589-024-01565-w
- Kim, D., Herdeis, L., Rudolph, D., Zhao, Y., Böttcher, J., Vides, A., Ayala-Santos, C.I., Pourfarjam, Y., Cuevas-Navarro, A., Xue, J.Y., et al. (2023).
   Pan-KRAS inhibitor disables oncogenic signalling and tumour growth.
   Nature 619, 160–166. https://doi.org/10.1038/s41586-023-06123-3.
- Holderfield, M., Lee, B.J., Jiang, J., Tomlinson, A., Seamon, K.J., Mira, A., Patrucco, E., Goodhart, G., Dilly, J., Gindin, Y., et al. (2024). Concurrent inhibition of oncogenic and wild-type RAS-GTP for cancer therapy. Nature 629, 919–926. https://doi.org/10.1038/s41586-024-07205-6.
- 12. Jiang, J., Jiang, L., Maldonato, B.J., Wang, Y., Holderfield, M., Aronchik, I., Winters, I.P., Salman, Z., Blaj, C., Menard, M., et al. (2024). Translational



- and Therapeutic Evaluation of RAS-GTP Inhibition by RMC-6236 in RAS-Driven Cancers. Cancer Discov. *14*, 994–1017. https://doi.org/10.1158/2159-8290.CD-24-0027.
- Wasko, U.N., Jiang, J., Dalton, T.C., Curiel-Garcia, A., Edwards, A.C., Wang, Y., Lee, B., Orlen, M., Tian, S., Stalnecker, C.A., et al. (2024). Tumour-selective activity of RAS-GTP inhibition in pancreatic cancer. Nature 629, 927–936. https://doi.org/10.1038/s41586-024-07379-z.
- Zhou, B., Der, C.J., and Cox, A.D. (2016). The role of wild type RAS isoforms in cancer. Semin. Cell Dev. Biol. 58, 60–69. https://doi.org/10.1016/j.semcdb.2016.07.012.
- Sardh, E., Harper, P., Balwani, M., Stein, P., Rees, D., Bissell, D.M., Desnick, R., Parker, C., Phillips, J., Bonkovsky, H.L., et al. (2019). Phase 1 Trial of an RNA Interference Therapy for Acute Intermittent Porphyria. N. Engl. J. Med. 380, 549–558. https://doi.org/10.1056/NEJMoa1807838.
- Belgrad, J., Fakih, H.H., and Khvorova, A. (2024). Nucleic Acid Therapeutics: Successes, Milestones, and Upcoming Innovation. Nucleic Acid Ther. 34, 52–72. https://doi.org/10.1089/nat.2023.0068.
- Abdelaal, A.M., and Kasinski, A.L. (2021). Ligand-mediated delivery of RNAi-based therapeutics for the treatment of oncological diseases. NAR Cancer 3, zcab030. https://doi.org/10.1093/narcan/zcab030.
- Papke, B., Azam, S.H., Feng, A.Y., Gutierrez-Ford, C., Huggins, H., Pallan, P.S., Van Swearingen, A.E.D., Egli, M., Cox, A.D., Der, C.J., and Pecot, C. V. (2021). Silencing of Oncogenic KRAS by Mutant-Selective Small Interfering RNA. ACS Pharmacol. Transl. Sci. 4, 703–712. https://doi. org/10.1021/acsptsci.0c00165.
- Manoharan, M., Akinc, A., Pandey, R.K., Qin, J., Hadwiger, P., John, M., Mills, K., Charisse, K., Maier, M.A., Nechev, L., et al. (2011). Unique gene-silencing and structural properties of 2'-fluoro-modified siRNAs. Angew. Chem. Int. Ed. Engl. 50, 2284–2288. https://doi.org/10.1002/ anie.201006519.
- Egli, M., and Manoharan, M. (2023). Chemistry, structure and function of approved oligonucleotide therapeutics. Nucleic Acids Res. 51, 2529– 2573. https://doi.org/10.1093/nar/gkad067.
- Nair, J.K., Willoughby, J.L.S., Chan, A., Charisse, K., Alam, M.R., Wang, Q., Hoekstra, M., Kandasamy, P., Kel'in, A.V., Milstein, S., et al. (2014). Multivalent N-acetylgalactosamine-conjugated siRNA localizes in hepatocytes and elicits robust RNAi-mediated gene silencing. J. Am. Chem. Soc. 136, 16958–16961. https://doi.org/10.1021/ja505986a.
- Pecot, C.V., Wu, S.Y., Bellister, S., Filant, J., Rupaimoole, R., Hisamatsu, T., Bhattacharya, R., Maharaj, A., Azam, S., Rodriguez-Aguayo, C., et al. (2014). Therapeutic silencing of KRAS using systemically delivered siRNAs. Mol. Cancer Ther. 13, 2876–2885. https://doi.org/10.1158/1535-7163.mct-14-0074.
- Brown, C.R., Gupta, S., Qin, J., Racie, T., He, G., Lentini, S., Malone, R., Yu, M., Matsuda, S., Shulga-Morskaya, S., et al. (2020). Investigating the pharmacodynamic durability of GalNAc-siRNA conjugates. Nucleic Acids Res. 48, 11827–11844. https://doi.org/10.1093/nar/gkaa670.
- Foster, D.J., Brown, C.R., Shaikh, S., Trapp, C., Schlegel, M.K., Qian, K., Sehgal, A., Rajeev, K.G., Jadhav, V., Manoharan, M., et al. (2018).
   Advanced siRNA Designs Further Improve In Vivo Performance of GalNAc-siRNA Conjugates. Mol. Ther. 26, 708–717. https://doi.org/10. 1016/j.ymthe.2017.12.021.
- Hassler, M.R., Turanov, A.A., Alterman, J.F., Haraszti, R.A., Coles, A.H., Osborn, M.F., Echeverria, D., Nikan, M., Salomon, W.E., Roux, L., et al. (2018). Comparison of partially and fully chemically-modified siRNA in conjugate-mediated delivery in vivo. Nucleic Acids Res. 46, 2185–2196. https://doi.org/10.1093/nar/gky037.
- Conroy, F., Miller, R., Alterman, J.F., Hassler, M.R., Echeverria, D., Godinho, B.M.D.C., Knox, E.G., Sapp, E., Sousa, J., Yamada, K., et al. (2022). Chemical engineering of therapeutic siRNAs for allele-specific gene silencing in Huntington's disease models. Nat. Commun. *13*, 5802. https://doi.org/10.1038/s41467-022-33061-x.
- Al-Ghamdi, S., Albasri, A., Cachat, J., Ibrahem, S., Muhammad, B.A., Jackson, D., Nateri, A.S., Kindle, K.B., and Ilyas, M. (2011). Cten is tar-

- geted by Kras signalling to regulate cell motility in the colon and pancreas. PLoS One 6, e20919. https://doi.org/10.1371/journal.pone.0020919.
- Wislez, M., Fujimoto, N., Izzo, J.G., Hanna, A.E., Cody, D.D., Langley, R.R., Tang, H., Burdick, M.D., Sato, M., Minna, J.D., et al. (2006). High expression of ligands for chemokine receptor CXCR2 in alveolar epithelial neoplasia induced by oncogenic kras. Cancer Res. 66, 4198–4207. https://doi.org/10.1158/0008-5472.CAN-05-3842.
- Pecot, C.V., Calin, G.A., Coleman, R.L., Lopez-Berestein, G., and Sood, A. K. (2011). RNA interference in the clinic: challenges and future directions. Nat. Rev. Cancer 11, 59–67. https://doi.org/10.1038/nrc2966.
- Ahmadi, S., Sukprasert, P., Vegesna, R., Sinha, S., Schischlik, F., Artzi, N., Khuller, S., Schäffer, A.A., and Ruppin, E. (2022). The landscape of receptor-mediated precision cancer combination therapy via a single-cell perspective. Nat. Commun. 13, 1613. https://doi.org/10.1038/s41467-022-29154-2.
- Li, Z., Zhao, R., Wu, X., Sun, Y., Yao, M., Li, J., Xu, Y., and Gu, J. (2005). Identification and characterization of a novel peptide ligand of epidermal growth factor receptor for targeted delivery of therapeutics. FASEB J. 19, 1978–1985. https://doi.org/10.1096/fj.05-4058com.
- Genta, I., Chiesa, E., Colzani, B., Modena, T., Conti, B., and Dorati, R. (2017). GE11 Peptide as an Active Targeting Agent in Antitumor Therapy: A Minireview. Pharmaceutics 10, 2. https://doi.org/10.3390/pharmaceutics10010002.
- Lee, J.W., Choi, J., Kim, E.H., Choi, J., Kim, S.H., and Yang, Y. (2023).
   Design of siRNA Bioconjugates for Efficient Control of Cancer-Associated Membrane Receptors. ACS Omega 8, 36435–36448. https://doi.org/10.1021/acsomega.3c05395.
- Sorkin, A., and Duex, J.E. (2010). Quantitative analysis of endocytosis and turnover of epidermal growth factor (EGF) and EGF receptor. Curr. Protoc. Cell Biol. Chapter 15. Unit 15 14. https://doi.org/10.1002/0471143030. cb1514s46.
- Nair, J.K., Attarwala, H., Sehgal, A., Wang, Q., Aluri, K., Zhang, X., Gao, M., Liu, J., Indrakanti, R., Schofield, S., et al. (2017). Impact of enhanced metabolic stability on pharmacokinetics and pharmacodynamics of GalNAcsiRNA conjugates. Nucleic Acids Res. 45, 10969–10977. https://doi.org/ 10.1093/nar/gkx818.
- Bensch, F., Smeenk, M.M., van Es, S.C., de Jong, J.R., Schröder, C.P., Oosting, S.F., Lub-de Hooge, M.N., Menke-van der Houven van Oordt, C.W., Brouwers, A.H., Boellaard, R., and de Vries, E.G.E. (2018). Comparative biodistribution analysis across four different (89)Zr-monoclonal antibody tracers-The first step towards an imaging warehouse. Theranostics 8, 4295–4304. https://doi.org/10.7150/thno.26370.
- Haderk, F., Chou, Y.T., Cech, L., Fernández-Méndez, C., Yu, J., Olivas, V., Meraz, I.M., Barbosa Rabago, D., Kerr, D.L., Gomez, C., et al. (2024). Focal adhesion kinase-YAP signaling axis drives drug-tolerant persister cells and residual disease in lung cancer. Nat. Commun. 15, 3741. https:// doi.org/10.1038/s41467-024-47423-0.
- Rozengurt, E., and Eibl, G. (2021). Crosstalk between KRAS, SRC and YAP Signaling in Pancreatic Cancer: Interactions Leading to Aggressive Disease and Drug Resistance. Cancers (Basel) 13, 5126. https://doi.org/ 10.3390/cancers13205126.
- Shao, D.D., Xue, W., Krall, E.B., Bhutkar, A., Piccioni, F., Wang, X., Schinzel, A.C., Sood, S., Rosenbluh, J., Kim, J.W., et al. (2014). KRAS and YAP1 converge to regulate EMT and tumor survival. Cell 158, 171–184. https://doi.org/10.1016/j.cell.2014.06.004.
- Kapoor, A., Yao, W., Ying, H., Hua, S., Liewen, A., Wang, Q., Zhong, Y., Wu, C.J., Sadanandam, A., Hu, B., et al. (2014). Yap1 activation enables bypass of oncogenic Kras addiction in pancreatic cancer. Cell 158, 185–197. https://doi.org/10.1016/j.cell.2014.06.003.
- Edwards, A.C., Stalnecker, C.A., Jean Morales, A., Taylor, K.E., Klomp, J. E., Klomp, J.A., Waters, A.M., Sudhakar, N., Hallin, J., Tang, T.T., et al. (2023). TEAD Inhibition Overcomes YAP1/TAZ-Driven Primary and Acquired Resistance to KRASG12C Inhibitors. Cancer Res. 83, 4112– 4129. https://doi.org/10.1158/0008-5472.CAN-23-2994.

# **Cancer Cell**

### **Article**



- Hagenbeek, T.J., Zbieg, J.R., Hafner, M., Mroue, R., Lacap, J.A., Sodir, N. M., Noland, C.L., Afghani, S., Kishore, A., Bhat, K.P., et al. (2023). An allosteric pan-TEAD inhibitor blocks oncogenic YAP/TAZ signaling and overcomes KRAS G12C inhibitor resistance. Nat. Cancer 4, 812–828. https://doi.org/10.1038/s43018-023-00577-0.
- Amodio, V., Yaeger, R., Arcella, P., Cancelliere, C., Lamba, S., Lorenzato, A., Arena, S., Montone, M., Mussolin, B., Bian, Y., et al. (2020). EGFR Blockade Reverts Resistance to KRAS(G12C) Inhibition in Colorectal Cancer. Cancer Discov. 10, 1129–1139. https://doi.org/10.1158/2159-8290.CD-20-0187.
- Salmon, M., Alvarez-Diaz, R., Fustero-Torre, C., Brehey, O., Lechuga, C.G., Sanclemente, M., Fernandez-Garcia, F., Lopez-Garcia, A., Martin-Guijarro, M.C., Rodriguez-Perales, S., et al. (2023). Kras oncogene ablation prevents resistance in advanced lung adenocarcinomas. J. Clin. Investig. 133, e164413. https://doi.org/10.1172/ JCI164413.
- Li, D., Geng, K., Hao, Y., Gu, J., Kumar, S., Olson, A.T., Kuismi, C.C., Kim, H.M., Pan, Y., Sherman, F., et al. (2024). Targeted degradation of oncogenic KRASG12V triggers antitumor immunity in lung cancer models. J. Clin. Investig. 135, e174249. https://doi.org/10.1172/JCI174249.
- Matsuo, Y., Campbell, P.M., Brekken, R.A., Sung, B., Ouellette, M.M., Fleming, J.B., Aggarwal, B.B., Der, C.J., and Guha, S. (2009). K-Ras promotes angiogenesis mediated by immortalized human pancreatic epithelial cells through mitogen-activated protein kinase signaling pathways.
   Mol. Cancer Res. 7, 799–808. https://doi.org/10.1158/1541-7786.MCR-08-0577
- Awad, M.M., Liu, S., Rybkin, I.I., Arbour, K.C., Dilly, J., Zhu, V.W., Johnson, M.L., Heist, R.S., Patil, T., Riely, G.J., et al. (2021). Acquired Resistance to KRAS(G12C) Inhibition in Cancer. N. Engl. J. Med. 384, 2382–2393. https://doi.org/10.1056/NEJMoa2105281.
- Tanaka, N., Lin, J.J., Li, C., Ryan, M.B., Zhang, J., Kiedrowski, L.A., Michel, A.G., Syed, M.U., Fella, K.A., Sakhi, M., et al. (2021). Clinical acquired resistance to KRASG12C inhibition through a novel KRAS switch-Il pocket mutation and polyclonal alterations converging on RAS-MAPK reactivation. Cancer Discov. 11, 1913–1922. https://doi.org/10.1158/ 2159-8290.CD-21-0365.
- Zhao, Y., Murciano-Goroff, Y.R., Xue, J.Y., Ang, A., Lucas, J., Mai, T.T., Da Cruz Paula, A.F., Saiki, A.Y., Mohn, D., Achanta, P., et al. (2021). Diverse alterations associated with resistance to KRAS(G12C) inhibition. Nature 599, 679–683. https://doi.org/10.1038/s41586-021-04065-2.
- Xue, J.Y., Zhao, Y., Aronowitz, J., Mai, T.T., Vides, A., Qeriqi, B., Kim, D., Li, C., de Stanchina, E., Mazutis, L., et al. (2020). Rapid non-uniform adaptation to conformation-specific KRAS(G12C) inhibition. Nature 577, 421–425. https://doi.org/10.1038/s41586-019-1884-x.
- Mukhopadhyay, S., Huang, H.Y., Lin, Z., Ranieri, M., Li, S., Sahu, S., Liu, Y., Ban, Y., Guidry, K., Hu, H., et al. (2023). Genome-Wide CRISPR Screens Identify Multiple Synthetic Lethal Targets That Enhance KRASG12C Inhibitor Efficacy. Cancer Res. 83, 4095–4111. https://doi.org/10.1158/0008-5472.CAN-23-2729.
- Tsai, Y.S., Woodcock, M.G., Azam, S.H., Thorne, L.B., Kanchi, K.L., Parker, J.S., Vincent, B.G., and Pecot, C.V. (2022). Rapid idiosyncratic mechanisms of clinical resistance to KRAS G12C inhibition. J. Clin. Investig. 132, e155523. https://doi.org/10.1172/JCI155523.
- Maltas, J., Killarney, S.T., Singleton, K.R., Strobl, M.A.R., Washart, R., Wood, K.C., and Wood, K.B. (2024). Drug dependence in cancer is exploitable by optimally constructed treatment holidays. Nat. Ecol. Evol. 8, 147–162. https://doi.org/10.1038/s41559-023-02255-x.
- Corcoran, R.B. (2023). A single inhibitor for all KRAS mutations. Nat. Cancer 4, 1060–1062. https://doi.org/10.1038/s43018-023-00615-x.
- McCormick, F. (2020). Sticking it to KRAS: Covalent Inhibitors Enter the Clinic. Cancer Cell 37, 3–4. https://doi.org/10.1016/j.ccell.2019. 12.009.
- Burgess, M.R., Hwang, E., Mroue, R., Bielski, C.M., Wandler, A.M., Huang, B.J., Firestone, A.J., Young, A., Lacap, J.A., Crocker, L., et al. (2017).
   KRAS Allelic Imbalance Enhances Fitness and Modulates MAP Kinase

- Dependence in Cancer. Cell *168*, 817–829.e15. https://doi.org/10.1016/i.cell.2017.01.020.
- 57. Yan, H., Yu, C.C., Fine, S.A., Youssof, A.L., Yang, Y.R., Yan, J., Karg, D.C., Cheung, E.C., Friedman, R.A., Ying, H., et al. (2021). Loss of the wild-type KRAS allele promotes pancreatic cancer progression through functional activation of YAP1. Oncogene 40, 6759–6771. https://doi.org/10.1038/s41388-021-02040-9.
- Najumudeen, A.K., Fey, S.K., Millett, L.M., Ford, C.A., Gilroy, K., Gunduz, N., Ridgway, R.A., Anderson, E., Strathdee, D., Clark, W., et al. (2024).
   KRAS allelic imbalance drives tumour initiation yet suppresses metastasis in colorectal cancer in vivo. Nat. Commun. 15, 100. https://doi.org/10. 1038/s41467-023-44342-4.
- Dowdy, S.F. (2023). Endosomal escape of RNA therapeutics: How do we solve this rate-limiting problem? RNA 29, 396–401. https://doi.org/10. 1261/ma.079507.122
- Orellana, E.A., Abdelaal, A.M., Rangasamy, L., Tenneti, S., Myoung, S., Low, P.S., and Kasinski, A.L. (2019). Enhancing MicroRNA Activity through Increased Endosomal Release Mediated by Nigericin. Mol. Ther. Nucleic Acids 16, 505–518. https://doi.org/10.1016/j.omtn.2019. 04 003
- Borten, M.A., Bajikar, S.S., Sasaki, N., Clevers, H., and Janes, K.A. (2018).
   Automated brightfield morphometry of 3D organoid populations by OrganoSeg. Sci. Rep. 8, 5319. https://doi.org/10.1038/s41598-017-18815-8.
- Dobin, A., Davis, C.A., Schlesinger, F., Drenkow, J., Zaleski, C., Jha, S., Batut, P., Chaisson, M., and Gingeras, T.R. (2013). STAR: ultrafast universal RNA-seq aligner. Bioinformatics 29, 15–21. https://doi.org/10.1093/bioinformatics/bts635.
- Frankish, A., Diekhans, M., Ferreira, A.M., Johnson, R., Jungreis, I., Loveland, J., Mudge, J.M., Sisu, C., Wright, J., Armstrong, J., et al. (2019). GENCODE reference annotation for the human and mouse genomes. Nucleic Acids Res. 47, D766–D773. https://doi.org/10.1093/nar/gky955.
- Love, M.I., Huber, W., and Anders, S. (2014). Moderated estimation of fold change and dispersion for RNA-seq data with DESeq2. Genome Biol. 15, 550. https://doi.org/10.1186/s13059-014-0550-8.
- Zhu, A., Ibrahim, J.G., and Love, M.I. (2019). Heavy-tailed prior distributions for sequence count data: removing the noise and preserving large differences. Bioinformatics 35, 2084–2092. https://doi.org/10.1093/bioinformatics/btv895.
- Eisen, M.B., Spellman, P.T., Brown, P.O., and Botstein, D. (1998). Cluster analysis and display of genome-wide expression patterns. Proc. Natl. Acad. Sci. USA 95, 14863–14868. https://doi.org/10.1073/pnas.95. 25.14863
- Saldanha, A.J. (2004). Java Treeview–extensible visualization of microarray data. Bioinformatics 20, 3246–3248. https://doi.org/10.1093/bioinformatics/bth349.
- Subramanian, A., Tamayo, P., Mootha, V.K., Mukherjee, S., Ebert, B.L., Gillette, M.A., Paulovich, A., Pomeroy, S.L., Golub, T.R., Lander, E.S., and Mesirov, J.P. (2005). Gene set enrichment analysis: a knowledgebased approach for interpreting genome-wide expression profiles. Proc. Natl. Acad. Sci. USA 102, 15545–15550. https://doi.org/10.1073/pnas. 0506580102
- Liberzon, A., Subramanian, A., Pinchback, R., Thorvaldsdóttir, H., Tamayo, P., and Mesirov, J.P. (2011). Molecular signatures database (MSigDB) 3.0. Bioinformatics 27, 1739–1740. https://doi.org/10.1093/bio-informatics/btr260.
- Patro, R., Duggal, G., Love, M.I., Irizarry, R.A., and Kingsford, C. (2017). Salmon provides fast and bias-aware quantification of transcript expression. Nat. Methods 14, 417–419. https://doi.org/10.1038/nmeth.4197
- Ianevski, A., Giri, A.K., and Aittokallio, T. (2022). SynergyFinder 3.0: an interactive analysis and consensus interpretation of multi-drug synergies across multiple samples. Nucleic Acids Res. 50, W739–W743. https:// doi.org/10.1093/nar/gkac382.





- Li, S., Olson, W.K., and Lu, X.J. (2019). Web 3DNA 2.0 for the analysis, visualization, and modeling of 3D nucleic acid structures. Nucleic Acids Res. 47, W26–W34. https://doi.org/10.1093/nar/gkz394.
- Pettersen, E.F., Goddard, T.D., Huang, C.C., Couch, G.S., Greenblatt, D. M., Meng, E.C., and Ferrin, T.E. (2004). UCSF Chimera–a visualization system for exploratory research and analysis. J. Comput. Chem. 25, 1605–1612. https://doi.org/10.1002/jcc.20084.
- Rey, J., Murail, S., de Vries, S., Derreumaux, P., and Tuffery, P. (2023).
   PEP-FOLD4: a pH-dependent force field for peptide structure prediction in aqueous solution. Nucleic Acids Res. 51, W432–W437. https://doi.org/10.1093/nar/gkad376.
- Schirle, N.T., and MacRae, I.J. (2012). The crystal structure of human Argonaute2. Sci. Technol. Humanit. 336, 1037–1040. https://doi.org/10. 1126/science.1221551.
- Case, D.A., Babin, V., Berryman, J.T., Betz, R.M., Cai, Q., Cerutti, D.S., T. E. Cheatham, I., Darden, T.A., Duke, R.E., Gohlke, H., et al. (2014). AMBER 14.
- de Hoon, M.J.L., Imoto, S., Nolan, J., and Miyano, S. (2004). Open source clustering software. Bioinformatics 20, 1453–1454. https://doi.org/10. 1093/bioinformatics/bth078.



# **STAR**\*METHODS

### **KEY RESOURCES TABLE**

	SOURCE	IDENTIFIER
Antibodies		
Rabbit monoclonal EGFR	Epitomics	Cat #AC-0025
Mouse monoclonal anti-vinculin	Sigma	Cat #V9264 RRID: AB_10603627
Rabbit polyclonal anti-pERK1/2 (Y202/T204)	Cell Signaling Technology	Cat #4370 RRID: AB_2315112
Rabbit polyclonal anti-ERK1/2	Cell Signaling Technology	Cat #9102 RRID: AB_330744
Rabbit polyclonal anti-pS6 (S235/6)	Cell Signaling Technology	Cat #2211 RRID: AB_331679
Rabbit monoclonal anti-S6	Cell Signaling Technology	Cat #2317 RRID: AB_2238583
Rabbit monoclonal anti-pMEK1/2 (S221)	Cell Signaling Technology	Cat #2338 RRID: AB_490903
Mouse monoclonal anti-MEK1/2	Cell Signaling Technology	Cat #4694 RRID: AB_10695868
Rabbit monoclonal anti-pEGFR (Y1068)	Cell Signaling Technology	Cat #3777 RRID: AB_2096270
Rabbit monoclonal anti-EGFR	Cell Signaling Technology	Cat #4267 RRID: AB_2246311
Rabbit polyclonal anti-pYAP (S127)	Cell Signaling Technology	Cat #4911 RRID: AB_2218913
Rabbit polyclonal anti-pYAP (Y357)	Abcam	Cat #ab62751 RRID:AB_956486
Rabbit monoclonal anti-Cyclophilin B	Cell Signaling Technology	Cat #43603 RRID: AB_2799247
Anti-mouse HRP	Jackson ImmunoResearch	Cat #115-035-003 RRID: AB_10015289
Anti-rabbit HRP	Jackson ImmunoResearch	Cat #111-035-003 RRID: AB_2313567
Mouse monoclonal anti-KRAS	Sigma	Cat #WH0003845M1 RRID: AB_1842235
Rabbit monoclonal anti-HA	Cell Signaling Technology	Cat #3724 RRID: AB_1549585
BUV395 rat anti-mouse CD45	BD Biosciences	Cat#564279; RRID:AB_2651134; Clone:30-F11
BUV563 rat anti-mouse CD44	BD Biosciences	Cat#741227; RRID:AB_2870781; Clone:IM7
AF594 rat anti-mouse CD8a	BioLegend	Cat#100758; RRID:AB_2563237; Clone:53-6.7
AF700 rat anti-mouse CD3	BioLegend	Cat#100216; RRID:AB_493696; Clone:17A2
APC/Cy7 rat anti-mouse PD1	BioLegend	Cat#135224; RRID:AB_2563523; Clone:29F.1A12
PE mouse anti-mouse Granzyme B	BioLegend	Cat#372208; RRID:AB_2687032; Clone:QA16A02
PE/Cy5 mouse anti-mouse NK1.1	BioLegend	Cat#108716; RRID:AB_493590; Clone:PK136

(Continued on next page)



Continued				
REAGENT or RESOURCE	SOURCE	IDENTIFIER		
PerCP/Cy5.5 rat anti-mouse CD11b	BioLegend	Cat#101228; RRID:AB_893232; Clone:M1/70		
BUV805 rat anti-mouse CD4	BD	Cat#741913; RRID:AB_2871227; Clone:RM4-4		
APC rat anti-mouse FOXP3	ThermoFisher	Cat#17-5773-82; RRID:AB_469457; Clone:FJK-16s		
Rabbit polyclonal anti-YAP	Cell Signaling Technology	Cat #4912; RRID: AB_2218911		
Chemicals, peptides, and recombinant protein	s			
MycoAlert Detection Kit	ThermoFisher Scientific	Cat #LT07-418		
PPMI-1640	Gibco	Cat #11875-093		
Dulbecco's Modified Eagle's Medium (DMEM)	Gibco	Cat #11965-052		
Fetal Bovine Serum (FBS)	Avantor	Cat #89510-185		
McCoy's 5A	Corning	Cat #10-050-CV		
Eagle's Minimum Essential Medium (EMEM)	ATCC	Cat #30-2003		
PBS	Gibco	Cat #14190-250		
Matrigel	Corning	Cat #CLS354234		
Hanks' Balanced Salt Solution (HBSS)	Gibco	Cat #14025076		
Puromycin	Gibco	Cat #A11138-03		
Lipofectamine RNAiMAX	Invitrogen	Cat #13778150		
Lipofectamine 2000	ThermoFisher Scientific	Cat #11668027		
Polybrene	Sigma	Cat #TR-1003		
Novolink Polymer	Leica	Cat #RE7161		
Bond Dewax Solution	Leica	Cat #AR9222		
Bond Wash Solution	Leica	Cat #AR9590		
Bond-Epitope Retrieval Solution	Leica	Cat #AR9961		
Cytoseal 60	Epredia	Cat #8310-4		
RIPA Buffer	ThermoFisher Scientific	Cat #89901		
HALT protease and phosphatase nhibitor cocktail	ThermoFisher Scientific	Cat #78440		
SuperBlock Blocking Buffer	ThermoFisher Scientific	Cat #37581		
TBS .	Thermo Scientific	Cat #J60877.K3		
Tween 20	Thermo Scientific	Cat #BP337-500		
Tris-Glycine Running Buffer	Thermo Scientific	Cat #J61006.K2		
Ory Milk Powder	RPI	Cat #M17200-500		
Гrypsin	Gibco	Cat #25200-072		
Frizol	ThermoFisher Scientific	Cat #15596026		
Glycogen	ThermoFisher Scientific	Cat #AMG9510		
Fris-Glycine SDS	Invitrogen	Cat #LC2676		
NuPAGE Sample Reducing Agent	Invitrogen	Cat #NP009		
RMC-7977	ChemGood	Cat #C-1010		
Cetuximab	BioXcell	SIM0002		
Гатохіfen	Millipore Sigma	Cat #T5648		
Opti-MEM	Gibco	Cat #31985-070		
LIVE/DEAD Fixable Blue Dead Cell Stain Kit	Invitrogen	Cat#L34961		
Collagenase Type I	Worthington Biochemical	Cat#NC9633623		
HEPES 1M	Corning	Cat#25-060-CI		

(Continued on next page)



Continued		
REAGENT or RESOURCE	SOURCE	IDENTIFIER
L-glutamine	Thermo Fisher	Cat# 25030081
BD Horizon Brilliant Stain Buffer	BD Biosciences	Cat#566349
Penicillin-Streptomycin	Cytiva HyClone	Cat #SV30010
Critical commercial assays		
Bond Intense R detection system	Leica	Cat #DS9263
miRNAscope RED Kit	Advanced Cell Diagnostics	Cat #324600
Quick RNA MiniPrep Zymo Research Kit	Zymo Research	Cat #R1055
2X PowerUp SYBR Green Master Mix	Life Technologies	Cat #100029284
BCA Assay	ThermoFisher Scientific	Cat #A55864
SuperSignal West Pico PLUS	Thermo Scientific	Cat #34580
Restore PLUS Western Blot Stripping Buffer	Thermo Scientific	Cat #46430
CellTiter-Glo 2.0 Cell Viability Assay	Promega	Cat #G9243
Luc-Pair Duo-Luciferase HT Assay Kit	Genecopoeia	Cat #LF015
Novex Tris-Glycine Mini Protein Gels	Invitrogen	Cat #XP04202BOX
TaqMan MicroRNA Reverse Transcription Kit	Applied Biosystems	Cat #4366596
TaqMan Universal Master Mix II	Applied Biosystems	Cat # 4440040
eBioscience Foxp3/Transcription Factor Staining Buffer Set	Invitrogen	Cat#00-5523-00
iScript cDNA Synthesis Kit	Bio-Rad	Cat #1708891
Deposited data		
Cancer Cell Line Encyclopedia		https://depmap.org/portal/ccle/
Protein Data Bank		https://www.rcsb.org/
NCI-H441 RNA-sequencing	This paper	GEO: GSE278018
NCI-H727 RNA-sequencing	This paper	GEO: GSE278019
SKCO-1 RNA-sequencing	This paper	GEO: GSE278020
Mendeley Raw Western Blot Data	This paper	https://doi.org/10.17632/sbb397pkvc.1
Experimental models: Cell lines		
NCI-H441	ATCC	Cat #HTB-174 RRID: CVCL_1561
NCI-H727	ATCC	Cat #CRL-5815 RRID: CVCL_1584
SKCO1	ATCC	Cat #HTB-39 RRID: CVCL_0626
A431	ATCC	Cat #CRL-1555 RRID: CVCL_0037
HCT116	ATCC	Cat #CCL-247
HEK293T	ATCC	Cat #CRL-3216 RRID: CVCL_0063
NCI-H358	ATCC	Cat #CRL-5807 RRID: CVCL_1559
Capan-2	ATCC	Cat #HTB-80 RRID: CVCL_0026
MPK195	Barbacid Lab DOI: 10.1172/JCl164413	
LU65	Hata Lab	RRID: CVCL_1392
Oligonucleotides		
SR-siRNA-KRASG12V-S1 probe	Advanced Cell Diagnostics	Cat #1206608-S1
SR-siRNA-KRASG12V-S1 probe miRNAscope positive control probe	Advanced Cell Diagnostics Advanced Cell Diagnostics	Cat #1206608-S1 Cat #727878-S1

(Continued on next page)



Continued		
REAGENT or RESOURCE	SOURCE	IDENTIFIER
qPCR Human KRAS For: TCCAACAATAGAGGATTCCTACAG	This paper	N/A
qPCR Human KRAS Rev: CCCTCATTGCACTGTACTCCT	This paper	N/A
qPCR Human DUSP6 For: TCCCTGAGGCCATTTCTTTCATAGATG	This paper	N/A
qPCR Human DUSP6 Rev: GCAGCTGACCCATGAAGTTGAAGT	This paper	N/A
qPCR Human GAPDH For: GGAGCGAGATCCCTCCAAAAT	This paper	N/A
qPCR Human GAPDH Rev: GGCTGTTGTCATACTTCTCATGG	This paper	N/A
qPCR Mouse KRAS For: CAAAGACAAGACAGAGAGTGGAG	This paper	N/A
qPCR Mouse KRAS Rev: TTCAATCTGTACTGTCGGATCTC	This paper	N/A
qPCR Mouse GAPDH For: AGTATGACTCCACTCACGGCAA	This paper	N/A
qPCR Mouse GAPDH Rev: TCTCGCTCCTGGAAGATGGT	This paper	N/A
qPCR Mouse Beta-Actin For: GGTCATCACTATTGGCAACG	This paper	N/A
qPCR Mouse Beta-Actin Rev: ACGGATGTCAACGTCACACT	This paper	N/A
EFTX-G12V SL-RT Primer: GTCGTATCCAGTGCAGG GTCCGAGGTATTCGCAC TGGATACGACTTGTGG	This paper	N/A
EFTX-G12V SL-qPCR For: ACTATCGCCAACAGCTCC	This paper	N/A
EFTX-G12V SL-qPCR Rev: CCAGTGCAGGGTCCGAGGTA	This paper	N/A
EFTX-G12V SL-qPCR Taqman Probe: (6FAM)TGGATACGACTTGTGGT(MGB)	This paper	N/A
Pan-KRAS siR SL-RT Primer: GTCGTATCCAGTGCAGGGTC CGAGGTATTCGCACTGGATA CGACCTGTCT	This paper	N/A
Pan-KRAS siR SL-qPCR For: GCGAGCTCGAGAATATCC	This paper	N/A
Pan-KRAS siR SL-qPCR Rev: CCAGTGCAGGGTCCGAGGTA	This paper	N/A
Pan-KRAS siR SL-qPCR Taqman Probe: (6FAM)TGGATACGACCTGTCTC(MGB)	This paper	N/A
Recombinant DNA		
pBABE-puro-KRAS	Genecopoeia	Cat #HCP288420-SG01-1-10
LentiCRISPRv1	Addgene	Cat #49535
pCL10A-1		
pBABE-puromycin		
Software and algorithms		
LICOR ImageStudio	LICOR Bio	Version 5.5.4
GraphPad Prism	GraphPad	Version 10
Organoseg	Borten et al. <sup>61</sup>	
Cary WinUV	Agilent Technologies	Version 3.0



Continued				
REAGENT or RESOURCE	SOURCE	IDENTIFIER		
FlowJo software v10.10.0	BD	https://www.flowjo.co/		
SpectroFlo software	Cytek	https://www.omiq.ai/		
STAR	Dobin et al. <sup>62</sup> https://github.com/alexdobin/STAR	Version 1.4.0		
GENCODE	Frankish et al. 63 https://www.gencodegenes.org/human/ releases.html	Release 22 and Release 36		
R	https://www.R-project.org/	Version 4.2		
DESeq2	Love et al. 64 https://bioconductor.org/packages/ release/bioc/html/DESeq2.html	Version 1.36.0		
apeglm	Zhu et al. 65 https://bioconductor.org/packages/ release/bioc/html/apeglm.html	Version 1.18.0		
Human Genome Organization (HUGO) Database	https://en.wikipedia.org/wiki/HUGO_ Gene_Nomenclature_Committee			
Cluster	Eisen et al. <sup>66</sup> http://bonsai.hgc.jp/~mdehoon/software/ cluster/	Version 3.0		
Treeview	Saldanha, AJ. <sup>67</sup> http://bonsai.hgc.jp/~mdehoon/software/ cluster/	Version 1.2.0		
Gene Set Enrichment Analysis (GSEA)	Subramanian et al. <sup>68</sup> https://www.gsea-msigdb.org/gsea/ index.jsp	Version 4.3.2		
Molecular Signature Database (MSigDB)	Liberzon et al. <sup>69</sup> https://www.gsea-msigdb.org/gsea/ msigdb/index.jsp	Version 2003.2		
Salmon	Patro et al. <sup>70</sup> https://github.com/COMBINE-lab/salmon	Version 2.7.6a		

#### **EXPERIMENTAL MODEL AND STUDY PARTICIPANT DETAILS**

## **Cell lines and culture conditions**

Cell lines were obtained from the ATCC and routinely tested for mycoplasma using a Lonza MycoAlert Detection kit (LT07-418). H441 (male), H727 (female) and H358 (male) cells were grown in RPMI-1640 containing 10% Fetal Bovine Serum (FBS) and 1% Penicillin–Streptomycin (P-S) antibiotic. SKCO1 (male) cells were grown in Eagle's Minimum Essential Medium (EMEM) with 10% FBS and 1% P-S. Capan2 (male) cells were grown in McCoy's 5A media with 10% FBS and 1% P-S. A431 (female) KRAS-knockout cells were previously described. <sup>18</sup> The murine lung adenocarcinoma MPK195<sup>44</sup> (kindly obtained from the Barbacid lab) cells were grown in Dulbecco's Modified Eagle's Medium (DMEM) media with 10% FBS and 1% P-S. A431 KRAS-knockout cells were transduced with lentiviral constructs expressing KRAS:Firefly Luciferase/Renilla Luciferase (Genecopoeia) control and then selected and maintained in puromycin (1  $\mu$ g/ml). LU65 (kindly obtained from the Hata lab) were grown in RPMI-1640 media with 10% FBS and 1% P-S. HCT116 cells were grown in McCoy's 5A medium with 10% FBS and 1% P-S. All cell lines were grown at 37°C with 5% CO<sub>2</sub>/95% air.

A431 cells overexpressing HA-tagged human *KRAS* wild-type and mutants were generated by first removing the endogenous *KRAS*<sup>WT</sup> gene using CRISPR/*Cas*9 and then transducing A431 cells with retroviral particles packaged with the same pBABE-puro-KRAS plasmids as previously described.<sup>18</sup> In short, a plasmid expressing KRAS sgRNA (atccGTAGTTGGAGCTGGTGGCGTGTTTTTAGAGCTAGAAAAAGTGGCACCGAGTCGGTGCTTTTTT, GeneCopoeia, catalogue # HCP288420-SG01-1-10) and a plasmid expressing *Cas*9 (Addgene Plasmid 49535) were co-transfected into A431 cells via the Neon Electroporation Transfection system (Thermo Fisher Scientific) as per the manufacturer's instructions. CRISPR/*Cas*9 knockout clones were generated using single cell cloning and screened via PCR and sanger sequencing to identify clones with successful removal of the endogenous *KRAS* gene. One such clone (Clone 2-10) was transduced with retrovirus expressing either *KRAS*<sup>WT</sup> or respective *KRAS* mutations. Retroviral particles were generated as follows: 1.25 μg pBABE-puromycin retroviral vectors overexpressing each *KRAS* isoform was cotransfected with 1.25 μg/μl PCL10A pack vector using 6.25 μg Lipofectamine 2000 (ThermoFisher Scientific) into HEK293T cells seeded in a 6 cm cell culture plate per the manufacturer's instructions. At 24 hours post transfection, the media on the HEK293T cells was changed to fresh media. Viral supernatant was collected





24 hours later and filtered. A431 cells were seeded in 6-well plates and 1 ml of virus was added along with 10  $\mu$ g/ml polybrene to each well to transduce for 48 hours at 37 °C. Virus was removed and 24 hours later selection media containing 1  $\mu$ g/ml puromycin was added to the cells. Cells were considered selected once all non-transduced cells in a control well were killed by the selection media.

#### In vivo modeling and tissue processing

Animals were cared for according to guidelines set forth by the American Association for Accreditation of Laboratory Animal Care and the U.S. Public Health Service policy on Human Care and Use of Laboratory Animals. Mouse studies were approved and supervised by the University of North Carolina at Chapel Hill Institutional Animal Care and Use Committee. Athymic female nude mice were between 8-12 weeks of age at the time of injection. H727, H441, SKCO1, H358, MPK195, Capan2 and A431 cells were trypsinized, washed and resuspended in Hanks balanced salt solution (HBSS; Gibco), and  $1x10^6$  (MPK195),  $2.5x10^6$  (A431),  $3x10^6$  (H358),  $3.5x10^6$  (H727 and H441) or  $5x10^6$  (SKCO1 and Capan2) cells were injected subcutaneously in a  $50~\mu$ Ls 1:1 mixture of HBSS and Matrigel (Corning). MPK195 cells were injected in mixed Sv129/B6 obtained from Jackson Labs (strain: 101043). Caliper measurements of subcutaneous tumor growth were taken twice weekly, and tumor volume was calculated as L x W² where L is the greatest cross-sectional length across the tumor and W is the length perpendicular to L. Once tumors reached  $\sim 100-150~mm^3$  in volume, mice were randomly assigned to their corresponding treatment groups. For SKCO1 combination experiment with pharmaceutical grade cetuximab, and cetuximab was dosed at 50~mpk twice weekly intraperitoneally.

#### **METHOD DETAILS**

#### siRNA transfections

The sequences of all siRNAs are in Table S6 and as previously described. All siRNA transfection experiments were completed using Lipofectamine RNAiMAX (Life Technologies) in culture media without antibiotics following manufacturer instructions.

### **GE11C** conjugation to siRNAs

Conjugation of GE11C to siRNAs was performed at either Avecia or Synoligo. Briefly, 3' aminated oligonucleotides (ONs) were made using an Oligo Synthesizer starting with Amino C6 CPG and purified by AEX HPLC (pH 11) with final purity more than 95%, followed by lyophilization to yield a white powder. Bi-functional linker, Mal-PEG3-NHS, was dissolved in anhydrous DMF (concentration 0.5 M). Quantified 3' Aminated ONs were dissolved in 0.1 M PBS (pH 7.4) to 600 OD/ml (20 mg/ml). Every 30 min Mal-PEG3-NHS solution (0.5 Equiv. of ONs) was added into PBS for conjugation under stirring until the completion of the reaction which was monitored by LC/MS. The reaction was stopped by addition of saturated sodium perchlorate solution in acetone and the 3' Mal-PEG3 modified ONs were precipitated and washed twice with acetone followed by evaporation of the organic solvent. The dried Mal-PEG3 modified ONs were dissolved in 0.1 M PBS (pH 7.4) to 600 OD/ml, and GE11C peptide (1.2 Equiv of ONs) was introduced into the aqueous solution for conjugation which was monitored by LC/MS until the end of reaction. The final reaction solution mixture was applied to RP HPLC for purification to obtain the target peptide-ONs conjugates.

## Immunohistochemistry and in situ hybridization

Immunohistochemical staining and in situ hybridization were performed in the Pathology Services Core Facility at the University of North Carolina at Chapel Hill. Chromogenic IHC for EGFR was performed on formalin-fixed paraffin-embedded tissues that were sectioned to 5 mm. Staining was performed on the Leica Bond III Autostainer system. Briefly, slides were dewaxed in Bond Dewax solution (Leica, AR9222) and hydrated in Bond Wash solution (Leica, AR9590). Heat induced antigen retrieval was performed at 100°C in Bond-Epitope Retrieval solution 1 pH-6.0 (Leica, AR9961) for 20 minutes. After pretreatment, slides were incubated with the rabbit monoclonal EGFR primary antibody (Epitomics, Cat # AC-0025) at 1:300 for 30 minutes followed by incubation with Novolink Polymer (Leica, RE7161) secondary. CD8a IHC was performed using a rabbit monoclonal CD8a primary antibody (Cell Signaling, Cat #98941) at 1:200 for 60 minutes, and phospho-ERK1/2 using a rabbit monoclonal antibody (Cell Signaling Technology, Cat # 4376) at 1:200 for 15 minutes. IHC staining detection with 3,3'-diaminobenzidine (DAB) and hematoxylin counterstain of the nuclei were performed using the Bond Intense R detection system (Leica, DS9263). Stained slides were dehydrated, and cover slipped with Cytoseal 60 (Epredia, 8310-4). Both positive and negative controls were included in these assays. siRNA-KRAS in situ hybridization was performed on formalin-fixed paraffin-embedded tissues that were sectioned to 5 mm. Slides were dewaxed in Bond Dewax solution (Leica, AR9222) and hydrated in Bond Wash solution (Leica, AR9590). Tissues were hybridized with customized SRsiRNA-KRASG12V-S1 probe (Advanced Cell Diagnostics, 1206608-S1). Signal detection was accomplished using miRNAscope RED Kit (Advanced Cell Diagnostics, 324600). A miRNAscope positive control probe (Advanced Cell Diagnostics, 727878-S1) and negative control probe (Advanced Cell Diagnostics, 727888-S1) were used to confirm signal and RNA integrity. Stained slides were digitized using the Aperio AT2 scanner (Leica Biosystems) at 40x magnification. The images were stored and analyzed in the Aperio eSlide Manager (eSM). Images for pERK, CD31 and CD8 IHC were taken in a blinded manner at 20x magnification and automated scoring using CellProfiler v4.2.8 was used to determine positive cells per high powered field. To obtain EGFR H-scores for the evaluated xenograft models we utilized QuPath v0.5.1.



#### **Quantitative reverse transcriptase PCR**

Total RNA from cell lysates was purified using the Quick RNA MiniPrep Zymo Research Kit (Zymo Research Cat # R1055). For mRNA analyses, cDNA was synthesized using the iScript cDNA Synthesis Kit (Bio-Rad, Cat # 1708891) as per the manufacturer's instructions. Analysis of RNA levels was determined by a StepOnePlus Real-Time PCR System (Applied Biosystems) using 2X PowerUp SYBR Green Master Mix (Life Technologies, # 100029284). A list of gene-specific primers used for RT-qPCR is included in the key resources table. Reactions were run in duplicate or triplicate. Fold change was calculated using the 2<sup>-ΔΔCT</sup> method and experiments were normalized to *GAPDH* or 18S RNA. Graphs and statistics were generated using GraphPad Prism.

#### Analysis of PK/PD studies using SL-RT-qPCR

Untreated tumor and plasma samples were used to generate standard curves for detection of EFTX-G12V antisense siRNA. Dilutions of EFTX-G12V siRNA were spiked into TRIzol following lysis and dissociation of tissues. Total RNA was isolated and used to generate a standard curve using antisense-stem-loop (AS-SL) qPCR. Stem-loop cDNA was synthesized with gene specific stem-loop primers, 300 ng total RNA, and the TaqMan MicroRNA Reverse Transcription Kit (Applied Biosystems, Cat #4366596) following the manufacturer's protocol. Analysis of EFTX-G12V siRNA was determined using TaqMan Universal Master Mix II (Applied Biosystems, Cat #4440040) and custom TaqMan primer and probe sets. Primer and probe sequences is included in the key resources table. The standard curve range of EFTX-G12V in A431-G12V-HA tumors was 0.1 – 183,000 ng/g, for plasma was 1.536 – 24,000 ng/ml and for kidney was 0.1 – 143,312 ng/g. Total RNA from experimental samples was analyzed using this method and total siRNA concentration was determined using the appropriate standard curves.

#### **Western blotting**

Cells were washed with ice cold PBS, lysed in RIPA buffer (Thermo Scientific Cat # 89901) supplemented with Halt protease and phosphatase inhibitor cocktail (Thermo Fisher Scientific Cat # 78440), scraped and collected in pre-chilled tubes. Lysates were then sonicated with a Fisherbrand Model 50 Sonic Dismembrator at 30 amp with 2-3 short pulses, repeated twice with lysates kept on ice between sonication. Lysates were then cleared by centrifugation at 14,000 g for 10 minutes, and protein concentration was determined using a BCA assay (Thermo Scientific Cat # A55864). Standard immunoblotting procedures were followed. Membranes were blocked in either 5% milk in TBS + 0.05% Tween 20 (TBST) or SuperBlock™ Blocking Buffer (Thermo Scientific Cat # 37581) for one hour at room temperature. Primary antibody dilutions ranged from 1:100 − 1:1,000 and were incubated overnight at 4°C. Antibodies are listed in the key resources table. Membranes were then washed three times with TBS-T and re-probed with the appropriate horseradish peroxidase-conjugated secondary antibodies (anti-mouse (#115-035-003) or anti-rabbit (#111-035-003) from Jackson ImmunoResearch) for one hour at room temperature. Membranes were then washed three times in TBS-T and developed using SuperSignal West Pico PLUS (Thermo Scientific Cat # 34580) and visualized with a LI-COR Odyssey Fc Imager. Blots were first imaged for phosphorylated targets, then stripped with Restore PLUS Western Blot Stripping Buffer for 10 minutes at room temperature. Blots were re-blocked and then incubated with corresponding total protein targets. Band intensities were quantified with ImageStudio. Relative band intensities were calculated in comparison to control siRNA-treated cells at the comparative dose and normalized to total protein as measured by vinculin or cyclophilin B expression.

#### **Cell viability experiments**

Cell viability in response to siRNA treatment was evaluated with the CellTiter-Glo 2.0 Cell Viability Assay (total cellular ATP assay) using the manufacturer's protocol (Promega). Resuspended cells in culture media were seeded in opaque, white, flat bottom 96-well plates. All siRNAs (suspended in serum-free media with Lipofectamine RNAiMAX) were tested in triplicate starting at 40 or 20 nM and progressing through a 10-point serial dilution. Plates were incubated in culture conditions for 5-8 days depending on the cell line. For viability readouts, 120 µl of media was removed from each well and an equal volume of CellTiter Glo 2.0 (CTG) Reagent was added. Luminescence was measured on a Synergy2 fluorescent plate reader (BioTek). Data was analyzed in GraphPad Prism.

### **Bliss Independence synergy evaluation**

For synergy evaluation, H727 and SKCO1 cells were seeded at 7,000 and 20,000 cells, respectively. EFTX-G12V siRNA was added to the cells at Day 0, starting at 40 or 24 nM and progressing through an 8-point serial dilution. At Day 3, cells were treated with DMSO or serial dilutions of RMC-7977 (starting from 25 or 400 nM), and cell viability readouts were measured at Day 6 using the CellTiter-Glo Luminescent Cell Viability Assay (Promega, G7573). A total of 3–4 biological replicates were done for each cell line. Synergy maps were generated for each cell line using the Bliss Independence method in SynergyFinder 3.0.<sup>71</sup> Four-parameter drug response curves and relative cell viability heatmaps were generated from biological replicates in GraphPad Prism.

#### **Luciferase experiments**

Changes in KRAS-Firefly Luciferase expression in response to siRNA treatment were evaluated with the Luc-Pair™ Duo-Luciferase HT Assay Kit using the manufacturer's protocol (Genecopoeia). Resuspended cells in culture media were added to opaque, flat bottom 96-well plates. A-431 KRAS-luciferase cells were seeded at 3,500 cells/well and were counted manually with a hemocytometer. All siRNAs (suspended in serum-free media with Lipofectamine RNAiMAX) were tested in triplicate starting at 40 or 20 nM and progressing through a 10-point serial dilution. Plates were incubated in culture conditions for 3-4 days. For Luciferase readouts, 120 µl of





media was removed from each well and an equal volume of working FLuc reagent was added and incubated for ten minutes. Luminescence was measured at 530 nm excitation and 590 nm emission on a Synergy2 fluorescent plate reader (BioTek). An equal volume of working RLuc reagent was subsequently added and incubated for an additional five minutes, and luminescence was measured as above. The ratio of luminescence from the Firefly Luciferase to the Renilla Luciferase was then calculated. Data was analyzed in GraphPad Prism and GI<sub>50</sub> curves were produced. Relative potency was calculated by dividing the GI<sub>50</sub> value of the pan-KRAS treated cells with the  $GI_{50}$  value of the other conditions.

#### 3D spheroid formation assay

H727, H441 and SKCO1 cells were seeded into 12-well plates and treated with 20 nM of siRNAs and Lipofectamine RNAiMAX in culture media without antibiotic for 24 hours. Cells were then lifted with Trypsin and counted manually with a hemocytometer. 5,000 cells from each condition were mixed with 50 µl of cold Matrigel (Corning) and plated onto 24-well glass bottom plates. After solidification of the matrix, complete media with 10% FBS and 1% P-S was added to every well. Plates were incubated for 8 days and then imaged with a Leica DMi8 inverted microscope (5x objective). Spheroid area and number in each condition were quantified using the Organoseg software. 19 Normalized spheroid area and number were used to generate combination index. Graphs were generated using GraphPad Prism.

#### **Spectral flow cytometry**

Tumors were excised immediately following CO<sub>2</sub> euthanasia. Tumors were cut into 1 mm pieces and digested for 30 mins at 37°C in RPMI-1640 containing 100U/mL Collagenase I (Worthington), 1 mM CaCl2, 1 mM MgCl2, 5 mM HEPES, 2 mM glutamine, and 5% FBS (Avantor). Suspensions were filtered through 70 micron strainers and resuspended in RPMI-1640 with 5% FBS. Cell suspensions were stained for 10 minutes at room temperature for viability with 1:800 LIVE/DEAD Fixable Blue (Invitrogen) plus 1:800 FcR block (BioLegend) in PBS protected from light in 96-well v-bottom plates (Costar). Extracellular master mix was prepared 2X in BD Horizon Brillant Stain Buffer (BD Bioscience) and added directly to cells suspensions for 30 minutes on ice and protected from light. Next cells were washed once with FACS (PBS plus 2% FBS) and fixed/permeabilized using the Foxp3/Transcription factor kit per manufacturer protocols (eBioscience). Intracellular targets were stained for 45 minutes on ice and protected from light. Cell pellets were washed and collected on a Cytek Aurora 5L spectral flow cytometer, unmixed, and analyzed using FlowJo v10 (BD).

For cytometry analysis, viable single cell lymphocytes were identified using forward and side scatter gates followed by doublet discrimination and negative staining for LIVE/DEAD Fixable Blue. Cytotoxic immune populations were defined as the frequency of granzyme B (GzmB) within the following populations: tumor reactive CD8 T cells (CD45\*CD3\*CD8a+CD44+PD1+), tumor reactive CD4 (CD45+CD3+CD4+Foxp3-CD44+PD1+), mature NK (CD45+CD3-NK1.1+CD11b+), NKT (CD45+CD3+CD4-CD8a-NK1.1+) and γδT cells (CD45+CD3+CD4-CD8a-NK1.1-). Statistical comparisons by testing for normality and equal variance followed by twoway ANOVA with Tukey's multiple comparisons. Significance was defined as \*\*\*\*p < 0.0001, \*\*\*p < 0.005, \*\*p < 0.01, and \*p < 0.05.

## Pharmacokinetic and pharmacodynamic studies in tumors and tissues

A431-G12V-HA, H441 and SKCO1 xenograft tumors and murine somatic tissues were collected from a cross-sectional necropsy of athymic mice treated with GE11-conjugated siRNAs and snap-frozen in liquid nitrogen. All tumors and tissues were stored at -80°C until processed. For RNA, tumors and murine somatic tissues were dissected on dry ice and RNA was isolated from 40-60 mg of tissue using Trizol® Reagent (Thermo Fisher Scientific Cat # 15596026) according to manufacturer instructions with the following alterations: tumors were lysed in 1 ml of Trizol® Reagent using a bead mill (speed: 3.7 m/s, time: 00:30 s, frequency: 7 times, incubating at 4°C for 2 min between each pulse), 30 µg of RNase free glycogen was added to the isolated aqueous layer as a co-precipitant, RNA was precipitated in an equal volume of isopropanol at -20°C for 20 mins, RNA pellet was washed twice in 75% EtOH, and resuspended in nuclease-free water.

For protein, tumors were dissected on dry ice and protein was isolated from 40-60 mg of tissue using RIPA buffer (Thermo Scientific Cat # 89901) supplemented with Halt protease and phosphatase inhibitor cocktail (Thermo Fisher Scientific Cat # 78440). Tumors were lysed in 600 ml lysis buffer using a bead mill (speed: 2.1 m/s, time: 00:30 s, incubating at 4°C for 2 min between each pulse) until tumors were fully lysed. Lysates were incubated at 4°C on a rocker for 20 minutes with full inversion every 5 minutes, followed by a brief ten second vortex, and then incubated at room temperature for 5 minutes. Lysates were then sonicated with a Fisherbrand Model 50 Sonic Dismembrator at 30 amp with 2-3 short pulses, repeated twice with lysates kept on ice between sonication. Lysates were then cleared by centrifugation at 14,000 g for 10 minutes, and protein concentration was determined using a BCA assay (Thermo Scientific Cat # A55864). Immunoblotting was completed as previously described.

## KRAS<sup>G12V</sup> siRNA duplex and conjugation modeling

We used 3DNA http://web.x3dna.org/index.php/fibermodel<sup>72</sup> to build the RNA KRAS<sup>G12V</sup> AS: S A-form duplex model and UCSF Chimera<sup>73</sup> to incorporate all chemical modifications: 5'-[mg]\*[2flc]\*[mc][ma][ma][2flc][ma][mg][mc][mc][mc][mc][mc][ma][2fla][mc][2flu] [mc]-amC6-3' (m=2'-O-methyl-ribonucleotide, 2fl=2'-deoxy-2'-fluoro-ribonucleotide, and \*=phosphorothioate). The GE11C ligand amino acid sequence is YHWYGYTPQNVIC. The 3D model of the peptide was generated and energy-minimized with PEP-FOLD4 https://bioserv.rpbs.univ-paris-diderot.fr/services/PEP-FOLD4/.74 The 3D rendering of the fully chemically modified KRAS<sup>G12V</sup> siRNA duplex with the conjugated GE11C EGFR peptide is depicted in Figure 3. Nitrogen, oxygen, hydrogen, 2'-O-methyl carbon, 2'-fluorine



and PS and Cys-13 sulfur atoms are colored in blue, red, white, yellow, green, and goldenrod, respectively. The color codes for nucleotide, linker and peptide carbon atoms are as follows: AS siRNA, light blue; S siRNA, beige; Mal-PEG3-NHS-aminohexyl linker, pink; and peptide, purple.

#### **UV** melting experiments

RNA duplexes were prepared by mixing solutions with equimolar concentrations of two strands (1.0  $\mu$ M) in 1 mL of 0.25 $\times$  PBS buffer, 34 mM NaCl, 0.7 mM KCl, 2.5 mM Na<sub>2</sub>HPO<sub>4</sub> and 0.5 mM KH<sub>2</sub>PO<sub>4</sub>, pH 7.4. Prior to running UV melting experiments, strands were annealed by heating samples in a water bath to 85°C for 2 min, followed by slow cooling to room temperature and 4C overnight. All measurements were made using a Cary 100 Bio UV—vis spectrophotometer (Agilent Technologies Inc., Santa Clara, CA), equipped with a temperature controlled multicell holder (6  $\times$  6) and a Cary temperature controller. Absorbance versus temperature profiles were acquired by monitoring the absorbance at 260 nm (A260) between 15°C and 90°C with a ramp rate of 0.5°C per minute. A<sub>260</sub> values were measured at 0.5°C intervals and melting temperatures T<sub>m</sub> were extracted as the maxima of the first derivatives of smoothened melting curves (filter 5) using the Cary WinUV software (Version 3.0, Agilent Technologies Inc.). T<sub>m</sub> values are averages of three independent experiments.

#### Modeling of the seed region of G12V AS-siRNA paired with G12V, wt-KRAS or G12D mRNA and bound to Argonaute2

Coordinates of the crystal structure of human Argonaute2 (Ago2) bound to guide and passenger RNA were retrieved from the Protein Data Bank http://www.rcsb: PDB ID 4w5t. <sup>75</sup> Bases of the guide strand were changed to those in the sequence of the G12V siRNA (AS1 – AS14; Figure 2) along with backbone modifications in the UCSF Chimera suite, <sup>73</sup> using the swapna and build/modify functions. Those of the passenger strand were replaced with bases that are either fully complementary to the guide seed region, AS5 G12V A:U (Figure 2B), or feature a single mismatch pair, AS5 wt A:G (Figure 2C) and AS5 G12D A:A (Figure 2D). All water molecules were removed and the *KRAS* <sup>G12V</sup>, <sup>-WT</sup> and <sup>-G12D</sup> Ago2 "guide siRNA:mRNA" complex models were subjected to energy minimization with Amber (ff14) using the steepest descent and conjugate gradient modes until convergence. <sup>76</sup> In Figure 2, carbon atoms of residues paired opposite KRAS AS5 A, U (*G12V*), G (*WT*) and A (*G12D*), are highlighted in red, goldenrod, and purple, respectively. Carbon atoms of the remaining residues in the guide and target strands are colored in light blue and tan, respectively, and H-bonds are shown as thin solid lines. 2'-O-Methyl groups and 2'-fluorine modifications of the guide siRNA are shown in ball-and-stick mode and are colored in yellow (carbon), white (hydrogen) and green (fluorine). Ago2 is depicted as a ribbon cartoon in gray with some key side chains that interact with the RNA duplex in the seed region highlighted in ball-and-stick mode: K709, R710, R714, and R761 that contact AS6 to AS8 phosphate groups, and I365, I756 and Q757 that line the minor groove. I365 is associated with a strong kink between AS6 and AS7 that is indicated by bold solid lines in Figure 2B.

#### **QUANTIFICATION AND STATISTICAL ANALYSIS**

## Bioinformatics and statistical analyses of RNA sequencing data of the SKCO1 cell line

Illumina RNA sequencing (RNA-Seq) FASTQ paired-end files produced by the Illumina NextSeq 2000 sequencing system [URL: Illuminal were, for each sample, jointly used. The alignment to the hg38 human reference genome was performed through STAR 2.7.6a (-outSAMunmapped Within; -outSMtype BAM Unsorted; -quantMode TranscriptomeSAM). 62 The quantification of transcripts was carried out using Salmon 1.4.0, 70 based on the human transcriptome defined by GENCODE, Release 22.63 Then, through a summary process, it was created a cohort-wide matrix showing the expression of the complete set of gene IDs of all samples. Thereafter, samples were processed, in order to remove gene IDs with lower average counts across sequenced samples, thus restricting the expression matrix to gene IDs (of all gene types) belonging to the upper fourth decile (value rounded by excess) of the two comparisons of interest (control siRNA vs. G12V siRNA and control siRNA vs. pan-KRAS siRNA), separately. We performed a differential expression analysis of rounded count data through DESeq2 (1.36.0), 64 within the R (4.2) software environment. Specifically, we collected base-Mean, p-value, and adjusted p-value (padj) using the 'results' function of DESeq2, with alpha = 0.0001 (here treated as an a priori optimal threshold for statistical significance). Following authors' recommendations, we separately calculated gene fold changes (log2 fold change) through the apeglm (1.18.0) R package, 65 to produce shrinkage estimators of effect sizes. Using the apeglm log2 fold changes and standard padj of DESeq2, we created volcano plots having, on the x-axis, log2(fold change) and, on the y-axis, -log10(padj) for all gene IDs tested. Null values for p-value and padj, according to the DESeq2 estimates, were replaced by the lowest values found in the analysis, conservatively. These plots were created using GraphPad Prism 9 [URL: GraphPad] and after removing genes (g(i)), i = 1,2,..., N, such that padj(g(i)) = NA, with N cardinality of the set of genes whose padj does not belong to the [0,1] interval.

Since the SKCO1 cell line is heterozygous for *KRAS*<sup>G12V</sup>, transcription from both alleles is typically expected. To generate estimates of the abundance of *KRAS*<sup>WT</sup> and *KRAS*<sup>G12V</sup> transcripts of our samples in different experimental conditions (control siRNA, pan-KRAS siRNA, and G12V siRNA), we used this algorithm: 1) we identified the nucleotide that is mutated between *WT* and *G12V* on the human chromosome 12 (chr12:25,245,350), in the region where *KRAS* is located. Then, in the BAM files of all samples (each based on the merging of Illumina R1 and R2 data), we quantified how many reads supported the *WT* (having a cytosine (C) in that position) and how many the *G12V* (having an adenine (A) in that position) *KRAS* forms; 2) we used these values to proportionally split the total *KRAS* counts between *WT* and *G12V*, separately in each sample. Then, while keeping the count values of all other genes unmodified, we produced a new count matrix having the same number of columns/samples, but with an extra row (one entry for





KRAS-WT and one for KRAS-G12V). After this split, we ran again DESeq2 on rounded count values and produced additional output variables, and in particular distinct padj and fold changes for the two KRAS forms. This simplified and approximate statistical approach assesses the two KRAS forms among all other analyzed genes, which are treated as mere genomic background of the analysis. Due to the smaller baseline values produced by the split before applying DESeq2, this model tends to be statistically conservative for the gene of interest (here, KRAS). We displayed these additional KRAS results, after removing the results of all other genes, by means of volcano plots with one data point for KRASWT and one for KRASG12V, both for the comparison control siRNA vs. pan-KRAS siRNA and for control siRNA vs. G12V siRNA.

#### Bioinformatics and statistical analyses of RNA-Seq data of the H441 and H727 cell lines

RNA-Seq count data, starting from the Illumina FASTQ files (NovaSeq 6000 sequencer), were produced similar to what we described for the SKCO1 cell line (see the previous paragraph), except for the use of the human transcriptome defined by GENCODE, Release 36.63 Thereafter, samples were processed, in order to remove gene IDs with lower total counts across sequenced samples, thus restricting the expression matrix to gene IDs having at least 10 counts across the nine (3 Control (Cont), 3 pan-KRAS, and 3 G12V) experimental samples of each cell line. Then, we analyzed our data as done for SKCO1 cells using DESeq2 (see the previous paragraph), with the difference that alpha was set to 0.01, used as a threshold of statistical significance for the heat maps (see below). In the end, only coding genes recognized by the Human Genome Organization (HUGO) [URL: HUGO] and with an adjusted p-value < 0.01 were kept. Those genes were log2-transformed, mean centered, hierarchically clustered with respect to genes (matrix rows) using Cluster 3.0<sup>77,66</sup> and visualized with the Java-based program TreeView.<sup>67</sup> We then moved to a gene set-based statistical approach, using data normalized in a way that is more suitable for this type of analyses. Specifically, the normalization procedure was such that quantile (0.75) = 1000; null and missing values were removed before using the R quantile function.

Following current recommendations of the Gene Set Enrichment Analysis (GSEA) team<sup>68</sup> about minimum sample sizes for standard GSEA, we opted for a GSEA-Pre-Ranked (PR) approach, which is based on pre-ranked gene metrics, by means of GSEA v.4.3.2. The chosen metric was signal-to-noise (S2N). To make all cases tractable, we introduced a perturbation of 1.00E-7 for the two standard deviations used in the S2N formulas of each gene (all calculations being based on normalized counts), therefore eliminating NaN instances of S2N. Similar to what we did before, only HUGO coding genes were kept in the GSEA PR analysis, thus using a submatrix (with 18,930 genes) of the normalized gene expression matrix. Overall, this procedure took matrixes, which were (18930, 6) and made them into vectors (18930, 1) of S2N values. These vectors were used as GSEA-PR inputs through ranked list (rnk) files, where genes were sorted alphabetically. The two tested collections were Hallmark (H) and Curated gene sets (C2) of the Molecular Signatures Database (MSigDB), 69 both of version v2003.2. These two gene set collections were provided as input through gene matrix transposed (gmt) files. The GSEA-PR comparisons assessed a) the enrichment of EFTX-G12V vs. Control and b) the enrichment of EFTX-G12V vs. pan-KRAS, so that EFTX-G12V was always the experimental group for which enrichments or depletions were tested. We considered enriched a gene set whose genes are predominantly more highly expressed in EFTX-G12V and depleted (i.e., suppressed or negatively enriched) a gene set whose genes are predominantly less expressed in EFTX-G12V vs. the compared groups (Cont and pan-KRAS, respectively). GSEA-PR was run using the gene symbol identifiers with no collapsing. The enrichment statistic was weighted. The cutoff thresholds for gene set sizes were 15 and 500, at the lower and upper end, respectively. The enrichment score (ES) of a gene set measures the level of enrichment of that gene set; the normalized enrichment score (NES) has the same goal while accounting for differences in gene set sizes and for the presence of other gene sets used in the same analysis.<sup>68</sup> We reported as statistically relevant all gene sets having a false discovery rate (FDR) q-value < 0.25, assuming this threshold as the highest acceptable for broad post-GSEA-PR assessments. Among relevant or significant gene sets, we performed further refinements according to their relationships with the findings described in this article. Besides, we calculated the leading edges (LEs) of statistically significant/relevant gene sets, which correspond to all genes up to the inflection points of the enrichment plots, which drive the enrichment or depletion. Finally, we collected, for gene sets of interest: i) gene ranks (using the formula Rank = GSEA\_PR\_Rank + 1), ii) gene orders, in that gene set, after the ranking, iii) LE status (Yes/No), iv) pre-ranked metric, and v) running ES. This data allowed us to replot the enrichment plots and pre-ranked metric plots, using GraphPad Prism 10 [URL: GraphPad], to enhance the visibility of plotted variables. The results of our GSEA PR analyses are shown in Tables S2, S3, S4, and S5. In these tables, when the header reads 'C (Control) vs. T (Treatment)', it means that we assessed the enrichment of T with respect to C. Therefore, if a gene set has positive enrichment score (ES) and normalized enrichment score (NES), that gene set is enriched in T, while if a gene set has negative ES and NES, it is suppressed in T (i.e., it is negatively enriched in T or, equivalently, it is enriched in C).

## Statistical analyses

Between 5 and 10 mice were assigned per treatment group; this sample size gave approximately 80% power to detect a 50% reduction in tumor weight with 95% confidence. Results for each group were compared using Student's t-test (for comparisons of two groups) and analysis of variance (ANOVA) (for multiple group comparisons). The multiple hypothesis testing correction of these statistical results was made using the FDR. A p-value less than 0.05 was deemed statistically significant. For values that were not normally distributed (as determined by the Kolmogorov-Smirnov test), the Mann-Whitney rank sum test was used. All statistical tests were performed using GraphPad Prism 10 (GraphPad Software, Inc., San Diego, CA). All line and bar graphs represent mean values, and all error bars represent standard error of the mean (S.E.M.).